Advances in Synthetic Aperture, Compounded Plane Wave, and Spatially Encoded Excitation Techniques for Fast Ultrasonography

by

Kyle Kotowick

B.Sc.(Hons) Computer Science, University of British Columbia Okanagan, 2011

A THESIS SUBMITTED IN PARTIAL FULFILLMENT
OF THE REQUIREMENTS FOR THE DEGREE OF

Master of Applied Science

in

THE FACULTY OF GRADUATE STUDIES
(Electrical and Computer Engineering)

The University Of British Columbia
(Vancouver)

August 2013

Abstract

Ultrasonography offers subcutaneous imaging at a fraction of the cost of magnetic resonance imaging (MRI) and without the ionizing radiation of X-ray or computed tomography (CT) imaging. In addition, ultrasound imaging machines are compact and portable, and do not require any sort of specialized environment to function. Ultrasonography is, however, limited by the relatively slow speed of sound and standard beamforming can only achieve low imaging frame rates (20 - 80 frames per second). This restricts its use in a number of applications that would otherwise benefit greatly from its use. For example, transient elastography, 3-dimensional volumetric imaging, and Doppler sonography would all benefit from higher frame rates.

This thesis presents two new variations of fast imaging methods. The first is by combining two existing fast-imaging techniques, plane wave (PW) and synthetic aperture (SA), using an adaptive weighting algorithm to compound images generated from the techniques individually. This method improves image resolution and signal-to-noise ratio (SNR) without losing the higher frame rate of each, which is successfully demonstrated through experiments on a physical commercial ultrasound system. The second method for increasing frame rate involves two extensions on a spatial encoding technique proposed by Fredrik Gran and Jørgen Arendt Jensen in 2008; these extensions entailed implementing a compressed sensing algorithm to reduce the code length requirement presented in their paper and removing the non-imagable "deadzone" region that their method produces. These extensions are applicable for scenarios requiring high definition for a small set of high-reflectivity points in an otherwise dark region, such as intra-spinal needle guidance, and are demonstrated using the Field II ultrasound simulation software.

Preface

All work presented in this thesis was completed at the Robotics and Control Laboratory at the University of British Columbia, Point Grey Campus. The work described in this thesis was completed independently by the author, K. Kotowick, with advisor guidance from professors L. Lampe and R. Rohling.

The hardware and software discussed in Chapter 3 are commercially available (hardware) or open-source (software) products that the author did not contribute to.

A version of Chapter 4 has been published in the proceedings of the International Symposium on Biomedical Imaging 2013 as "Adaptive Compounding of Synthetic Aperture and Compounded Plane-Wave Imaging for Fast Ultrasonography" [20].

Table of Contents

List of Tables

List of Figures

Glossary

AC adaptively compounded

ADC analog-to-digital conversion

CPW compounded plane wave

CT computed tomography

DAS delay-and-sum

FIR finite impulse response

FPS frames per second

GPU graphics processing unit

MRI magnetic resonance imaging

PW plane wave

RF radio-frequency

SA synthetic aperture

SNR signal-to-noise ratio

SONIXDAQ Ultrasonix Data Acquisition Card

SONIXRP Ultrasonix Research Platform

TGC time-gain compensation

Acknowledgments

First and foremost, I would like to thank Rob and Lutz who riskily accepted me into a program I had little background in, but had faith in me and provided excellent guidance. Your commitment to this project was admirable and crucial to its completion.

A special thanks to my parents Dwain and Shelley for raising me to the person I am today and for convincing me to pursue academia. Their support and love has always been unconditional and without bounds.

Thank you to my labmates for the welcoming and entertaining environment, in particular to Caitlin Schneider for taking me under her wing and patiently answering my continual questions, and to the support staff at Ultrasonix for graciously handling my hectic requests for technical assistance.

Finally, the completion of this research would not have been possible without funding from the Natural Sciences and Engineering Research Council of Canada (NSERC) and from the University of British Columbia.

Chapter 1

Introduction

A relatively mature technology, ultrasound imaging has seen a strong resurgence in new research over the past decade. In the face of rising medical costs, ultrasonography offers subcutaneous imaging at a fraction of the cost of magnetic resonance imaging (MRI) and without the ionizing radiation of X-ray or computed tomography (CT) imaging. It provides portable, real-time imaging capability without the need for a specialized environment. As opposed to X-ray or CT, which require radiation shielding, and MRI, which requires multi-million dollar equipment and a metal-free environment, ultrasonography can be performed at extremely low cost in nearly any situation.

Unfortunately, due to the relatively slow speed of sound, ultrasonography suffers from low image frame rates. Images are acquired in vertical sections, which are then combined to form a full frame. To avoid interference only one of these sections can be acquired at a time, necessitating a long data acquisition phase. Depending on the specific technique used and the imaging depth, the frame rate generally falls in the 20 - 80 frames per second (FPS) range. This restriction hampers a number of potential applications that require higher frame rates to be fully functional, including 3-dimensional imaging, elastography, and Doppler sonography.

3-dimensional volumetric imaging, usually generated by the sweeping of a 1-D transducer array over a 2-D plane, generates an image from a number of 2-D "slices" which are combined into the final 3-D volume. As each 2-D slice must be

generated individually, this drastically reduces the frame rate of a 3-D volume generated from 20 - 80 slices to around 1 FPS, which is insufficient for imaging nearly any form of internal motion. For this technique of 3-D imaging to be fully effective, significantly higher frame rates than conventional systems offer are required.

Elastography is a technique for detecting hard tissue within soft tissue (usually for tumor detection)[1]. The tissue is vibrated at approximately 60 - 150 FPS and is imaged with ultrasound simultaneously. Hard tissue will remain rigid, while soft tissue surrounding it will compress with the vibrations. The strain on sections of tissue are measured to detect the rigid regions, which signify a possible tumor [24]. As specified by the Nyquist sampling theorem, in order to reconstruct the tissue vibration the sampling (imaging) must be conducted at twice the vibration rate (120 - 300 FPS). Improvements in ultrasound frame rate are often required to achieve this goal.

Doppler sonography is a technique for assessing the motion of structures (often blood) through tissue, specifically their velocity relative to the transducer. Modern ultrasound machines use pulsed Doppler, where the frequency shift is determined from the phase changes of a given sample between pulses (frequency is the change of phase over time). The frequency shift can then be used to determine the speed and direction of the movement of that sample, which is then visualized by a colour overlay on the ultrasound image. Pulsed Doppler can suffer from aliasing when the frequency of the motion being observed is greater than the frame rate of the ultrasound imaging, which can result in misleading or missing information. A higher frame rate ultrasonography method would be of great benefit for use with Doppler imaging.

Frame rate also determines the time required to generate a single image frame. This has drastic implications even on techniques that do not require a high frame rate. For imaging of fast-moving organs, such as the heart, if an image frame takes a long duration to create then the organ will have moved during data collection. For techniques that acquire frames in sections, such as conventional transmit beamforming (Section 2.1.5), this means that part of the frame will have been generated while the organ is in a specific position and orientation, while other parts of will have been generated after the organ has moved. This effect makes generating high-resolution images without blurring significantly more difficult. Higher

frame rate ultrasound methods mean that organs will move less during the imaging period, therefore providing a higher quality image with fewer restrictions on stationarity.

The frame rate of conventional ultrasound imaging is dependent on a number of factors and can be defined as, in frames per second,

$$\text{Frame Rate} = \frac{c}{2md}, \tag{1.1}$$

where d is the depth of the region to be imaged, m is the number independent transmit events per frame, and c is the speed of sound in the imaged tissue (which averages 1540 m/s in human tissue). For a given region of tissue to image c and d are constant, so methods to improve frame rate focus on decreasing the value of m. m can be reduced in two ways: (1) reduce the number of transmits required to form a full frame, or (2) have multiple transmits occur simultaneously to reduce the total time required.

Previously proposed methods for reducing the number or required transmits per frame (1) include plane wave (PW) imaging (Section 2.2.2) and synthetic aperture (SA) imaging (Section 2.2.1). The PW technique activates all elements of a transducer simultaneously to produce a planar acoustic wave instead of a conventional focused beam, which illuminates the entire region in a single transmit (up to 128x increase in frame rate). The SA technique activates only a single element at a time which allows for dynamic transmit beamforming as well as receive beamforming, thereby giving a substantially greater accuracy in image reconstruction. The higher accuracy and unfocused nature of the single element activation allow for image generation with far fewer transmits than conventional. Both of these, however, have significant disadvantages that do not allow them to be a complete replacement for conventional imaging (discussed in detail in their respective sections).

One previously proposed method for using multiple transmits simultaneously (2) is spatial encoding of ultrasound pulses (Section 2.2.3). Spatial encoding, a.k.a. coded excitation, is a method that allows for simultaneous transmit events that are activated with unique coded pulses. The received signals can then be separated using a decoding matrix to isolate the echoes that originated from each individual

transmit.

1.1 Thesis Objectives

The goal of the work in this thesis is to improve the frame rate of ultrasound imaging without significantly decreasing the image quality. This is achieved with two separate methods:

1. Combining existing PW and SA fast-imaging techniques using an adaptive weighting algorithm to compound images generated from the techniques individually, giving an improvement in image resolution and signal-to-noise ratio (SNR) without losing the higher frame rate.

2. Improving on Gran and Jensen's spatial encoding technique [9] to eliminate "deadzones" (non-imageable regions due to the half-duplex constraint of ultrasound transducers) by implementing a compressed sensing with partial decoding method. Compressed sensing allows for a drastic reduction in encoded pulse length, and partial decoding allows for estimation of reflectors in the deadzone.

1.2 Thesis Structure

The outline of this thesis is as follows: Chapter 2 provides a detailed and comprehensive background on ultrasound imaging, as well as a number of techniques that have been attempted in order to improve frame rate. Chapter 3 details the equipment and software used in the course of this research, including the Ultrasonix Research Platform (SONIXRP), the Ultrasonix Data Acquisition Card (SONIXDAQ) and the Field II ultrasound simulation software. Chapter 4 presents an original method for improving image quality of existing high frame rate methods (PW and SA) by adaptively combining them. Chapter 5 presents two original extensions of the work done by Gran and Jensen on spatial encoding for fast imaging [9]. Their method is enhanced by implementing compressed sensing algorithms with partial decoding to remove the "deadzone" caused by the ultrasound transducer element half-duplex constraint. Finally, Chapter 6 presents the conclusions of this thesis and describes the direction of future work on the subject.

Chapter 2

Background

The following chapter provides an overview to current conventional ultrasound imaging systems as well as an introduction to proposed fast-imaging techniques, as a basis for the original work described in Chapter 4 and Chapter 5.

2.1 Conventional Ultrasound Basics

2.1.1 Acoustic Wave Generation

Sound waves are generated from piezoelectric elements (devices that vibrate when a voltage is applied) arranged in a 1-D array, encased in a housing (the "transducer"). These elements are excited at the desired frequency by an impulse generator in the ultrasound machine. Imaging frequencies are generally selected on the basis of type and depth of tissue to be imaged, with higher frequencies giving better resolution but poorer tissue penetration than lower frequencies. A given transducer consists of elements that have a natural central frequency, usually in the range of 2 - 20 MHz (with exceptions for highly specialized applications). The frequency of the impulse generator is generally selected to correspond with the transducer's central frequency, with some leeway to force a specific frequency slightly higher or lower if desired. The impulses provided by the impulse generator can be positive or negative, with variable power levels available depending on the equipment (in the sense that the power level of the entire impulse sequence can be adjusted, but not

individual impulses within a transmit). Pre-programmed series of positive and negative impulses can be used to generate a specific pulse shape in the waveform, with applications for encoded transmits (coded excitation). The impulses received by the elements cause them to vibrate, thereby transmitting an acoustic wave into the tissue they are placed against. A specialized gel is used in between the transducer and tissue surface to minimize reflections from the transition.

2.1.2 Transducer Designs

Ultrasound transducers are available in a wide variety of designs for specific applications. Most commonly used for external imaging (where the transducer is against an exterior surface of the body) are convex (Figure 2.1a) and linear (Figure 2.1b) transducers. Convex transducers form an image with a wide field of view that increases with depth, but decreases in resolution (Figure 2.1c). Linear transducers form a rectangular image with more consistent resolution (Figure 2.1d), and are used exclusively for the experiments (both physical and simulated) described in this thesis.

2.1.3 Transmit Beamforming

Modern ultrasound machines use phased array transducers, which allow each elements to be fired independently with varying time delays [34, 46]. By varying the delays on each element, the ultrasound beam can be shaped or steered to focus on a given point. This is known as fixed transmit focusing. Doing so drastically increases the ratio of energy focused on that point versus all other points in the tissue, which simplifies the image formation calculations and provides higher accuracy.

For each focused transmit, a transmit aperture is defined (i.e., the number of elements transmitting). The transmit aperture is generally user-adjustable, depending on the application. A narrow aperture will provide a narrower beam above and below the focal point, while a wider aperture will have a wider beam but will provide more acoustic power at the focal point.

Conventional ultrasonography, commonly known as delay-and-sum (DAS) ultrasound, uses at least one transmit focused vertically on each element column. For each of these transmits, a small vertical section of the final image is generated, and

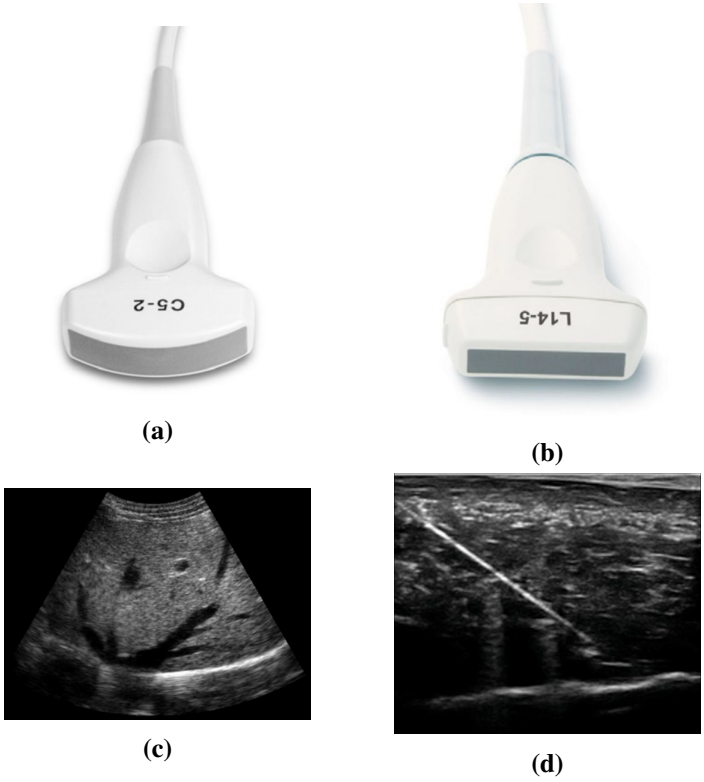

Figure 2.1: (a) An Ultrasonix C7-3 convex transducer. (b) An Ultrasonix L14-5 linear transducer. (c) Image generated by a convex transducer. (d) Image generated by a linear transducer. Images courtesy of Ultrasonix Medical Corp.

combined/stitched horizontally with the image sections from each other transmit.

Depending on the depth of the region of interest and level of quality desired, multiple transmit focuses may be done for each element column, with various focal depths. This results in image sections being combined/stitched both horizontally and vertically.

2.1.4 Echo Reception

Reflected sound waves are received in the reverse way that they are transmitted. Echoes transfer from the tissue into the transducer elements, causing them to vibrate and produce an electrical signal. The signal passes through analog-to-digital

conversion (ADC) hardware and the ultrasound machine captures the resultant digital signal and records it for use in generating the final image. The received signal is known as the radio-frequency (RF).

As acoustic waves travel through tissue, their power is attenuated. Therefore, received echoes that originated from reflectors at a lower depth will have a lower power than echoes that originated from reflectors of the same strength at a shallower depth. This effect is minimized by using time-gain compensation (TGC) which artificially increases the power of reflections based on the time they take to arrive at the receiving element [39], providing a more uniform and accurate brightness in the image.

2.1.5 Receive Beamforming and Aperture

When a transmitted acoustic wave is reflected by a point in the tissue, it scatters, meaning that the echo will be received by multiple elements in the transducer. Receive beamforming is the re-focusing of the received echoes for each point in the image being generated. For each point (x,z) in the image, the temporal coordinate of the corresponding signal in the received RF of a column-beamformed transmit (i.e., the transmit beam is perpendicular to the transducer face, and not steered) is given by

$$\tau(x_r, x, z) = \frac{z + \sqrt{z^2 + (x - x_r)^2}}{c}, \tag{2.1}$$

where x is also the lateral position of the transmit focus and x_r is the lateral position of the receiving element. For each given depth z (generally given in increments of the sampling interval) in each element column x, the corresponding temporal coordinate of the RF from each receiving element is calculated using Equation 2.1 and are then summed together to find the total value for that point in the image.

The piezoelectric elements used in ultrasound transducers are most receptive to vibrations traveling directly perpendicular to the surface of the element (axially), and the receptiveness decreases as the angle of the incoming reflected wave increases. Therefore, only elements within a certain distance from the element column the transmit is focused on are useful in receiving. To compensate for this, the receive aperture (i.e., the elements of the transducer that are used to contribute to

a given point (x,z) in the image) is determined by the depth (z) of that point. The width of the receive aperture is given by

$$D = Nz, \tag{2.2}$$

where D is the width of the aperture and N is the F-number. The F-number is simply the ratio of the focal length to the aperture width, and is usually (and for all experiments in this thesis) set to 0.5 with user-adjustability on ultrasound machines.

2.1.6 Image Formation

After receive beamforming is completed and the values for each point in the image have been summed, the RF is envelope-detected using a Hilbert transform to provide a displayable greyscale image. The image is often also logarithmically compressed to display a greater dynamic range and increase the visibility of smaller differences in reflection amplitude.

2.2 Fast Imaging Methods

A number of alternative imaging methods have been proposed and studied, with the intention of achieving a higher frame rate than conventional imaging.

2.2.1 Synthetic Aperture

SA imaging [18], based on the technique for radar systems [35], synthesizes an aperture by using a single element, moving it over the region of interest, and combining the resultant datasets. This technique offers the benefit of extremely high resolution; as only one element is transmitting at once, it is known exactly where a given reflection originated (as opposed to conventional transmit beamforming where a reflected signal could have come from any element in the transmit aperture), known as dynamic transmit focusing. Because of this high precision, the same resolution as conventional imaging can be achieved with fewer transmits, e.g., with transmits on every second element instead of a focus for each element with conventional. Fewer transmits translates to a higher frame rate, as shown in

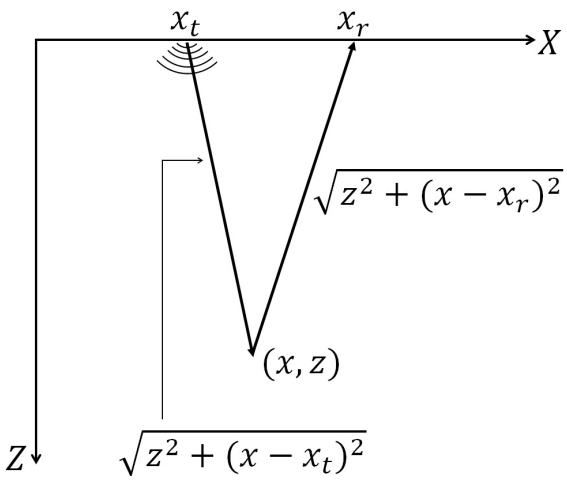

Figure 2.2: Time delays for an SA transmit from element at position x_t to a point (x,z) and received by element at position x_r.

Equation 1.1. The use of SA imaging for medical applications was first considered in the 1970s and 80s [2, 5, 27], and was developed with more advanced techniques over the following decades [14, 22, 23, 28].

The drawback to this method is that due to single-element transmits, and therefore the lower amount of acoustic energy entering the tissue per transmit, the received RF SNR is significantly lower than that of conventional imaging (i.e., details of the tissue being imaged are less visible among the background noise). Several methods have been proposed for overcoming this issue, which are described in Section 4.2.1.

2.2.2 Plane Wave

One method for obtaining high frame rates is that of PW imaging (Figure 2.3)[32, 33], where all transducer elements are fired together to create a quasi-planar wave. Due to the large number of elements firing per transmit, and therefore the large amount of energy illuminating the tissue, this method offers a relatively high SNR. On receive dynamic beamforming, reflections are assumed to have originated from the leading edge of the plane wave. Firing all elements simultaneously as opposed

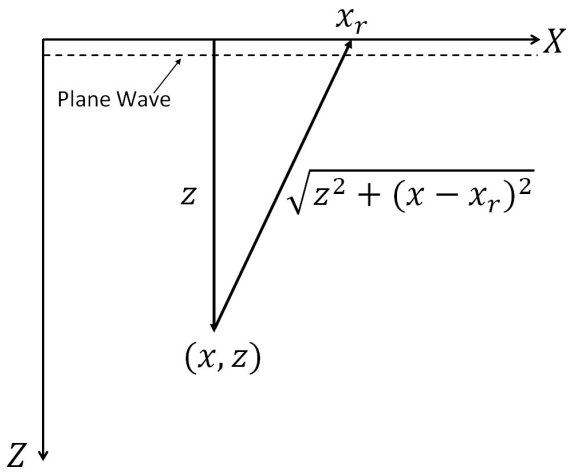

Figure 2.3: Time delays for a plane wave to a point (x, z) and received by element at position x_r.

to sequential focused columns allows an entire image to be generated from a single transmit event, leading to a frame rate over 100 times higher than conventional imaging (7500+ FPS for a 10cm deep image), making it particularly well suited for techniques requiring dynamic motion tracking such as transient elastography for cancer detection [1].

However, the lack of a transmit focus results in drastically lower resolution than conventional transmit beamforming techniques offer. Work has been done in the field to improve this drawback, as detailed in Section 4.2.2.

2.2.3 Coded Excitation

A more recent method for improving ultrasound frame rate, and one of the main foci of this thesis, is the use of coded excitation. In conventional ultrasound, only one group of elements is activated at a time, where "group" is defined as a set of elements that are programmed to have a common focal point. If more than one group is activated, then the origin of received echoes becomes ambiguous and causes a drastic drop in image quality. The theory behind coded excitation is based on the idea that it should be possible to have multiple transmits simultaneously that each transmit an individual code, which can be decoded and isolated in the

received RF. After isolation, they are treated in processing as if they were entirely separate.

Coded excitation presents the benefit of requiring $\frac{1}{K}$ as many transmits per image as conventional imaging, where K is the number of groups transmitting simultaneously with encoded pulse sequences. This directly translates to K times the frame rate as the equivalent conventional imaging, but with the drawback of decreased image quality due to the non-linear nature of tissue, as well as what is referred to in this thesis as a "deadzone", where tissue cannot be imaged due to the half duplex constraint of the transducer and the required length of encoded pulse sequences. These drawbacks and the proposed methods for minimizing or removing them (one of the objectives of this thesis) are described in Chapter 5.

Chapter 3

Equipment and Software

In this chapter are details and specifications for the equipment (SONIXRP and SONIXDAQ) used to perform the physical experiments in Chapter 4, and an overview of the software (Field II) used to perform the simulations in Chapter 5.

3.1 SonixRP

3.1.1 Specifications

The SONIXRP is a diagnostic ultrasound system from Ultrasonix Medical Corporation. The operating system consists of a customized version of Microsoft Windows XP, allowing for use of the machine in a PC-type manner. The SONIXRP supports 128-element transducers, with 256 transmit channels and 32 receive channels. The ultrasound system runs on a 40 MHz internal clock, and utilizes 10-bit ADC hardware.

3.1.2 Research Interface

The SONIXRP comes packaged with a research interface. The research interface and other special research tools on the RP allow for the the following additional functionality (as listed in Ultrasonix's documentation [45]):

1. The use of operational modes not available on a purely clinical system

Figure 3.1: The Ultrasonix Research Platform (SONIXRP). Image courtesy of Ultrasonix Medical Corp.

2. The retrieval and modification of low-level parameters used to generate ultrasound images
3. The acquisition and storage of raw data in a variety of formats
4. Transducer prototyping
5. Connecting to the system through a network for parameter setting and data capture
6. Low-level ultrasound beam sequencing and control
7. Development of commercial ultrasound applications running on the Sonix platform

For the research in this thesis, the most important of these were 2 and 6. Running experiments using SA and PW imaging requires control over the individual elements in the transducer and their parameters, including apertures, time delays, power, excitation pulse shapes, and TGC. Access to the entire operating system in research mode is also required for data collection using the SONIXDAQ, as described in Section 3.2, and for post-processing of said data using external applications such as Matlab or custom C++ applications.

3.2 SonixDAQ

3.2.1 Specifications

The Ultrasonix Data Acquisition Card (SONIXDAQ) is a device from Ultrasonix Medical Corporation that is designed to integrate with their ultrasound research platforms (Figure 3.2a). Where the research interface in the SONIXRP will allow the capture of receive beamformed RF data that is a summation of the individual channels, the SONIXDAQ captures the raw (pre-beamformed) RF data received by each individual element. It is a receive-only device that does not effect the imaging sequence in any way, but captures the data as it is gathered and stores it in internal memory. Raw RF data is processed through ADC hardware, high-pass filtered, packed into a usable format, and stored in memory. After the imaging sequence is complete, the raw RF data can be downloaded from the SONIXDAQ's internal memory to the SONIXRP's internal hard disk via a USB cable (Figure 3.2b). The SONIXDAQ supports 128 parallel receive channels (each with an independent ADC) and contains 16 GB of internal memory to store the RF data. It uses a 40 MHz internal clock, with support for both 40 MHz sampling (with 12-bit ADC) and 80 MHz sampling (with 10-bit ADC). It connects to one of the transducer ports on the ultrasound machine for transfer of the RF data (Figure 3.2d), and to an external trigger port on the ultrasound machine for synchronized data acquisition (the SONIXDAQ begins recording a new frame when the ultrasound machine signals that a new transmission has begun).

(a)

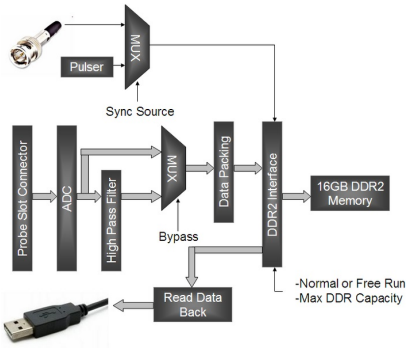

(b)

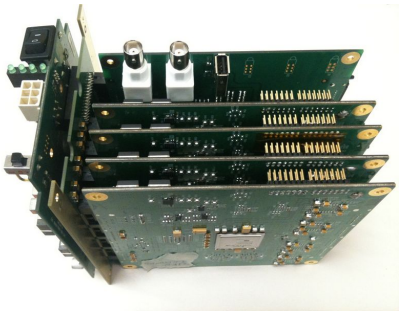

(c)

(d)

Figure 3.2: (a) A SONIXDAQ module. (b) A high-level block diagram showing the design of the SONIXDAQ. (c) The internal circuitry of the SONIXDAQ. (d) The SONIXDAQ installed on a SONIXRP ultrasound machine. Images courtesy of Ultrasonix Medical Corp.

3.2.2 Reasons for Requirement

Because the experiments in this thesis use element parameters and firing sequences that are entirely different than the conventional (default) ones for the SONIXRP, the raw RF data must be receive beamformed and processed in a different manner. This means that the beamformed RF data that is captured and stored by the SONIXRP is insufficient, and the SONIXDAQ module is therefore required for all of the experiments described in Chapter 4.

3.3 Field II

Field II is an ultrasound simulation program for use in Matlab, written by Jørgen Arendt Jensen, the first version of which was published in 1996 [17]. Field II runs simulations on a matrix representation of a phantom (an object specifically designed for use in medical imaging tests) which consists of a series of (x, y, z) coordinates of point reflectors, each with an accompanying reflection amplitude. Transducer specifications (including element width, kerf, depth, height, central frequency, impulse response, and number of elements) are given to model a physical transducer and its elements. Details of the simulation process can be found in the program's documentation [15], but a summary is given here. The software, built on a basis of linear systems theory, calculates the spatial impulse response for each given point in space as a function of time using the given transducer parameters and phantom matrix (this is based on research presented in [43], [37], and [36]). This spatial impulse response is initially calculated assuming a Dirac delta function is used as an excitation for the transducer elements. For other excitations, such as the coded excitations used in Chapter 5, the spatial impulse response from the Dirac excitation is simply convolved with the given excitation to find the new spatial impulse response. To calculate the final received RF, this new spatial impulse response is convolved with the impulse response of the receiving element and adjusted to compensate for the electro-mechanical transfer function of the transducer. Jensen cites proofs of this theory found in [38] and [31]. Apodization of elements (edges vibrating differently than the centre) is emulated by dividing the elements into squares, for each of which the received RF is calculated independently. The sum of the responses for these sub-elements gives the response of the entire ele-

ment. Further background on the theory behind Field II can be found in [16].

Chapter 4

Adaptive Compounding of Synthetic Aperture and Compounded Plane-Wave Imaging for Fast Ultrasonography

In this chapter, a novel technique is presented that combines two previously proposed fast-imaging techniques to achieve high frame rate ultrasonography with finer resolution and higher SNR than conventional imaging. The technique is tested on a physical ultrasound system to demonstrate its viability.

4.1 Background

Several imaging techniques have been proposed that provide for a higher physical frame rate limit by requiring fewer transmits per image frame. As described in Section 2.2.1, synthetic aperture (SA) imaging [18] synthesizes an aperture by using a single element, moving it over the region of interest, and combining the resultant datasets. Although the ability to dynamically focus in transmit provides a large boost in resolution SA suffers from an inherently low SNR due to the low num-

ber of element firings per frame, and therefore lower amount of acoustic energy entering the tissue, compared to conventional focused transmit beamforming.

Another method for obtaining high frame rates is that of plane wave (PW) imaging [32, 33], where all transducer elements are fired together to create a quasi-planar wave. As described in Section 2.2.2, due to the large number of elements firing per transmit this method offers a high SNR but the lack of a transmit focus results in significantly lower resolution than conventional transmit beamforming techniques offer. Nevertheless, the exceptionally high frame rates (7500+ FPS for a 10cm deep image) make it especially useful for dynamic motion tracking [1].

There is a need for combining the benefits of synthetic aperture and plane-wave imaging without compromising frame rate. It is anticipated that adaptively compounding the results of the two methods can maximize the resolution contributed by SA and the SNR contributed by PW without incorporating the negative side-effects of each.

4.2 Previous Research

4.2.1 Synthetic Aperture Imaging

Several methods have been proposed for overcoming the issue of low SNR with SA imaging. In [19], several transducer elements of a transducer phased array (as opposed to the standard single element) are pulsed with "defocusing" time delays to simulate a virtual point source originating behind the transducer surface while increasing the signal power. In [40], a technique is described that improves SNR by pulsing each element at a different frequency. Another method under extensive investigation is transmit coding [3, 4, 6, 7, 10, 25, 29], where excitation pulses are encoded or modulated to allow for longer pulses (greater signal energy) without loss in resolution.

4.2.2 Plane Wave Imaging

One of the most successful attempts to improve the resolution of PW imaging was by Montaldo *et al.* [26], who described a system for coherently compounding received signals from a number of plane waves transmitted at various angles called

compounded plane wave (CPW). In doing so, they achieved a resolution comparable to that of conventional transmit beamforming but still below that of SA imaging, while maintaining an exceptionally high SNR.

4.3 Experimental Design

Our proposed method is based on combining the strengths of SA and CPW imaging while minimizing the drawbacks. In doing so, better resolution and contrast are created without limiting the system to a lower frame rate than either method would provide individually. Frame rate is defined by

$$\text{Frame Rate} = \frac{c}{2md}, \tag{4.1}$$

where d is the depth of the region to be imaged, m is the number of transmits per frame, and c is the speed of sound in the imaged tissue. In this thesis, the proposed 128-transmit adaptively compounded (AC) method is compared against 128-transmit SA-only and CPW-only methods, as well as against a 256-transmit (two focal depths per element) conventional DAS beamformed transmit method. The final compounded image would be expected to improve lateral and axial resolution compared to CPW and increase SNR compared to SA imaging. Both resolution and SNR would be expected to be better than the conventional DAS technique at two focus depths, but with twice the frame rate.

4.3.1 Image Generation

To generate a compounded image, sparse images are first obtained from CPW and SA methods individually. The CPW image is formed by compounding the data of 64 PW transmits at varying steering angles, evenly distributed over a 33° range. The received signals are delay-and-sum beamformed, with the transmit-scatterer(x,z)-receiver delay defined as

$$\tau(\alpha, x_r, x, z) = \frac{z\cos\alpha + x\sin\alpha}{c} + \frac{\sqrt{z^2 + (x - x_r)^2}}{c}, \tag{4.2}$$

where α is the plane wave steering angle and x_r is the lateral position of the receiving element. This is the sum of the wave-to-scatterer travel time and the scatterer-

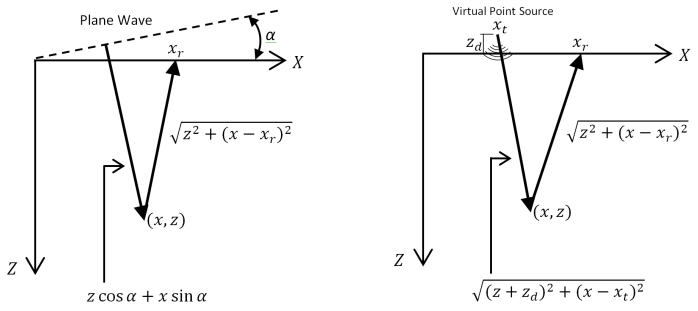

Figure 4.1: (a) Time delays for a plane wave of angle α to a point (x,z) and received by element at position x_r. (b) Time delays for an SA transmit from element at position x_t to a scatterer at (x,z) and received by element at position x_r.

to-receiver travel time, as can be seen in Figure 4.1a.

The SA image is then formed by compounding the data of 64 virtual-point-source transmits from evenly spaced transmit points across the transducer. This step uses the multi-element aperture method suggested in [19], where a defocused time delay curve simulates a point source behind the transducer. The time delay before firing of an element n in the aperture is defined as

$$\tau_n = \frac{x_n^2}{2z_d c}, \tag{4.3}$$

where x_n is the distance of the nth element from the aperture centre, z_d is the distance of the defocal point behind the aperture centre, and c is the speed of sound in the imaged tissue. As also suggested in [19], z_d is chosen to be $dK_t/2$, where d is the inter-element spacing and K_t is the aperture width (selected as 10 for this comparison). The received signals are then DAS receive beamformed, with the transmit-scatterer(x,z)-receiver delay defined as

$$\tau(x_t,x_r,z_d,x,z) = \frac{\sqrt{(z+z_d)^2+(x-x_t)^2}}{c} + \frac{\sqrt{z^2+(x-x_r)^2}}{c}, \tag{4.4}$$

where x_t is the lateral position of the virtual point source. This is the sum of the transmitter-to-scatterer travel time and the scatterer-to-receiver travel time, as can

be seen in Figure 4.1b.

The data from each of these images then undergoes standard post-processing, including a bandpass filter centered around the transmit frequency to remove background noise, and a Hilbert transform for envelope detection.

4.3.2 Adaptive Image Data Compounding

Once the sparse CPW and SA images have been obtained, they are compounded into a single high-quality frame. The objective is to retain the high SNR of the CPW image, while also retaining the high resolution of the SA image. This is done using an adaptive weighted averaging technique, where the CPW image is given preference for low-reflectivity regions (where SNR and contrast are most crucial) and the SA image is given preference for high-reflectivity regions (where sharply defined, highly reflective edges give strong echoes that are easily captured by SA). Each point $v(x,z)$ in the final image is generated according to the equation

$$v(x,z) = \frac{CPW(x,z)}{CPW_{max}} SA(x,z) + \left(1 - \frac{CPW(x,z)}{CPW_{max}}\right) CPW(x,z), \tag{4.5}$$

where CPW_{max} is the highest intensity point in the CPW image.

4.3.3 Physical Implementation

This system was implemented on a SONIXRP with a SONIXDAQ for capturing full-frame raw RF signals. The element transmit sequences were programmed using the Ultrasonix "Texo" software development kit for a 6 cm image at a frequency of 9.5 MHz, and the sequence was used on a CIRS General Purpose Multi-Tissue Ultrasound Phantom, Model 40 (CIRS, Norfolk, Virginia), as seen in Figure 4.2. Once RF data were captured for all transmit sequences, they were processed offline on a dual-core desktop workstation in a C++ application.

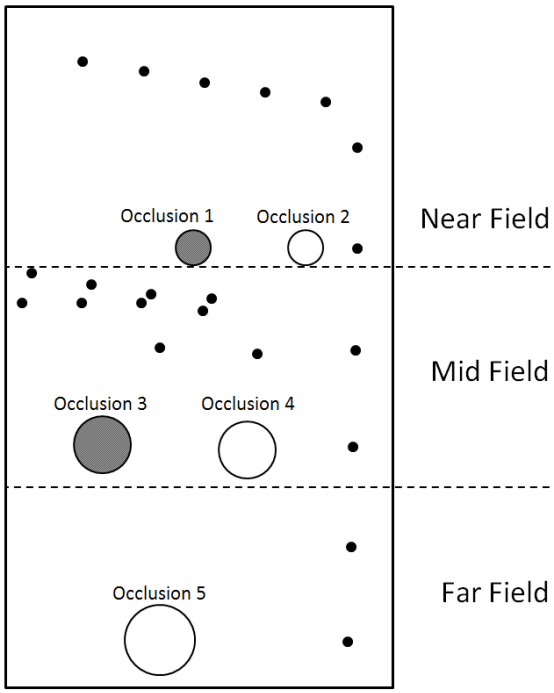

Figure 4.2: Structure of the CIRS General Purpose Multi-Tissue Ultrasound Phantom, Model 40.

4.4 Results and Discussion

The resulting images of the CPW, SA, AC, and conventional DAS (with focus depths at 2 cm and 4 cm) techniques, as seen in Figure 4.3, were compared according to their resolution in the near, mid, and far field, and their SNR in the occlusion regions of the phantom.

4.4.1 Resolution

The lateral and axial resolution of the techniques was measured at the full width at half maximum on the point spread response from the wire targets. Since the phantom background exhibited significant and variable speckle, the point spread function was defined as the width at half maximum of the values in the region of

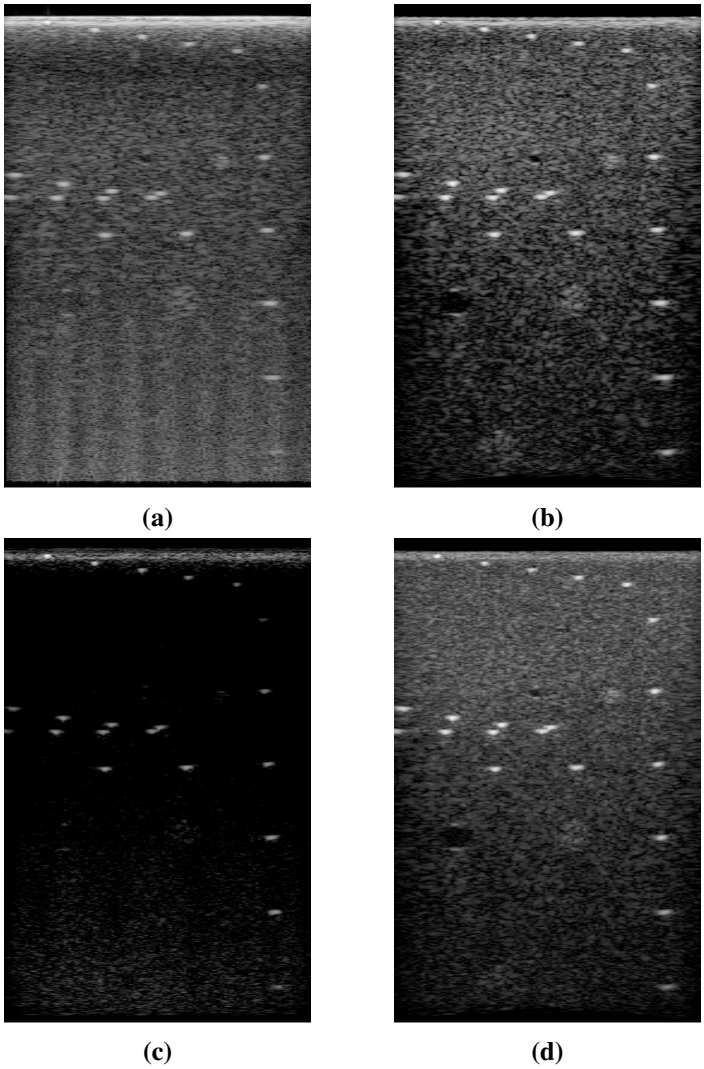

Figure 4.3: (a) B-mode conventional DAS transmit beamforming with 2 focal depths, 128 transmits each (256 total). (b) 128-transmit CPW with 128-element aperture. (c) 128-transmit SA with 10-element aperture. (d) Adaptively compounded 64-transmit CPW and 64-transmit SA.

interest minus the average value in the surrounding area. The function was applied in lateral and axial directions for each of 16 distinguishable point scatterers fully contained within the frame. These points were then divided into near, mid, and far fields, as seen in Figure 4.2. Tables 4.1 and 4.2 show the mean results for each field in the lateral and axial directions, respectively. As expected, the resolution of the compounded technique fell between those of the CPW and SA techniques, with an overall 14.5% gain over CPW, 12.8% gain over conventional, and 17% loss from SA in lateral resolution, and an overall 7.5% gain over CPW, 2.7% gain over conventional, and 14.7% loss from SA in axial resolution.

Table 4.1: Lateral Resolution (mm)

	DAS	CPW	SA	AC
Near Field	1.32	1.32	1.01	1.16
Mid Field	1.73	1.70	1.40	1.43
Far Field	2.02	2.16	1.37	1.83
Mean	1.69	1.72	1.26	1.47

Table 4.2: Axial Resolution (mm)

	DAS	CPW	SA	AC
Near Field	0.61	0.64	0.53	0.59
Mid Field	0.69	0.70	0.628	0.69
Far Field	0.72	0.78	0.56	0.69
Mean	0.67	0.71	0.57	0.66

4.4.2 Signal-to-Noise Ratio

The SNR of each technique was measured by comparing the values inside an occlusion to the values outside the occlusion, according to the equation

$$SNR(dB) = 10\log_{10}\frac{|\mu_{in} - \mu_{out}|}{\sqrt{\sigma_{in}\sigma_{out}}}, \tag{4.6}$$

where μ_{in} and σ_{in} are the mean value and standard deviation inside the occlusion, and μ_{out} and σ_{out} are the mean value and standard deviation in the area surrounding the occlusion. This function was applied to each of the five occlusions in the

imaged region (three high reflectivity, two low reflectivity). Table 4.3 shows the results. As expected, the occlusion SNR of the compounded technique fell between those of the CPW and SA techniques, with an overall 14.54 dB gain over SA, 4.85 dB gain over conventional, and 2.01 dB loss from CPW.

Table 4.3: Occlusion Imaging SNR (dB)

	DAS	CPW	SA	AC
Occlusion 1	3.45	4.79	-33.71	3.40
Occlusion 2	2.76	1.62	1.31	-0.04
Occlusion 3	-8.35	5.25	-21.98	4.44
Occlusion 4	-0.78	2.28	-0.44	1.16
Occlusion 5	-17.20	0.29	-13.71	-4.80
Mean	-4.02	2.84	-13.71	0.83

4.4.3 Statistical Significance

The resolution and SNR results were compared using a one-tailed Mann-Whitney U test to determine their significance. Table 4.4 shows the p-values for the compounded method's improvements over CPW in resolution, SA in SNR, and conventional DAS in both (p-values of decreases in quality shown in parentheses). As the values show, the improvement in lateral resolution over PW and DAS was statistically significant ($p < 0.05$), as was the improvement in SNR over SA. The losses in lateral resolution and SNR compared to SA and CPW, respectively, were not statistically significant. This demonstrates that the improvements of the compounded method significantly outweigh the losses. Results could possibly be improved further yet by implementing a more advanced weighting algorithm (for Equation 4.5) that is more resilient to the effects of outliers in the CPW image.

Table 4.4: Significance p-values: comparison of resolution and SNR of adaptively compounded (AC) method vs. others

	DAS	CPW	SA
AC Lat. Res.	0.0202	0.0269	(0.1198)
AC Ax. Res.	0.3385	0.1216	(0.0051)
AC SNR	0.2103	(0.1548)	0.0476

4.5 Summary

The proposed technique has been implemented and validated using an Ultrasonix Medical Corporation SONIXRP and SONIXDAQ for testing on a tissue-mimicking gel phantom, showing a 14.5% gain in lateral resolution over CPW, a 7.5% gain in axial resolution over CPW, and a 14.5 dB gain in SNR over SA. Each of DAS, CPW, and SA performed poorly in one or more tests. CPW performed worst in lateral and axial resolution, and SA performed worst in occlusion SNR. Conventional DAS performed second worst in all three tests. Only the adaptive compounded method performed well in all three tests, while still maintaining a frame rate of at least double that of the tested conventional imaging technique. This method improves the general applicability of high frame rate imaging, as it is the only one of the three tested techniques that outperforms conventional DAS imaging in all aspects.

Chapter 5

Compressed Sensing and Partial Decoding for Receive-Side Separation of Multiple Simultaneous Transmit Events

This chapter describes a method for high frame rate ultrasonography through spatially coded excitation. The work is presented as two novel extensions of work completed by Fredrik Gran and Jørgen Arendt Jensen.

5.1 Background

As detailed in Section 2.2.1, SA images are formed by conducting a series of single element transmits, usually one for each element in the transducer. These pulses are run sequentially in order to avoid cross-talk and interference between separate transmit events. If pulses from separate elements were transmitted simultaneously, ambiguity would be introduced in the receive beamforming step (Section 2.1.5) as to where a given RF echo originated in the tissue. In a SA transmit pulse from an element at x_t, the signal received by an element at x_r at a given time τ could have originated from a set of points in the tissue, i.e., any coordinate (x, z) where the following holds true:

$$\sqrt{z^2+(x-x_t)^2}+\sqrt{z^2+(x-x_r)^2}=\tau. \tag{5.1}$$

The effect of this can be seen for two different transmit elements at x_{t1} and x_{t2} in Figure 5.1a and Figure 5.1b; the RF value at time τ could have originated from any point along an arc. This is compensated for in receive beamforming, where the received signals from multiple elements are adjusted and combined to reduce the arc to a single point. When two elements (at x_{t1} and x_{t2}, respectively) transmit simultaneously, however, the ambiguity is greatly amplified. The RF value received by an element at x_r at a given time τ could have originated from twice as many possible tissue points, i.e., from any point (x,z) where the following holds true:

$$(\sqrt{z^2+(x-x_{t1})^2}+\sqrt{z^2+(x-x_r)^2}=\tau)\vee(\sqrt{z^2+(x-x_{t2})^2}+\sqrt{z^2+(x-x_r)^2}=\tau). \tag{5.2}$$

This will cause two arcs of possible reflection points (Figure 5.1c), which can no longer be compensated for with receive beamforming. Therefore, conventional ultrasound imaging has continued to use only a single element transmit at a time.

If a method could be devised, however, that can reliably transmit with K elements simultaneously and isolate their signals in the received RF, the frame rate of that technique could be increase K-fold over the same technique without multiple simultaneous transmits. One technique under research for solving this problem is known as "spatial encoding" where element excitation pulse sequences consist of a code, with a unique code for each element transmitting simultaneously. This chapter details the previous research in this area and the author's proposed methods and results.

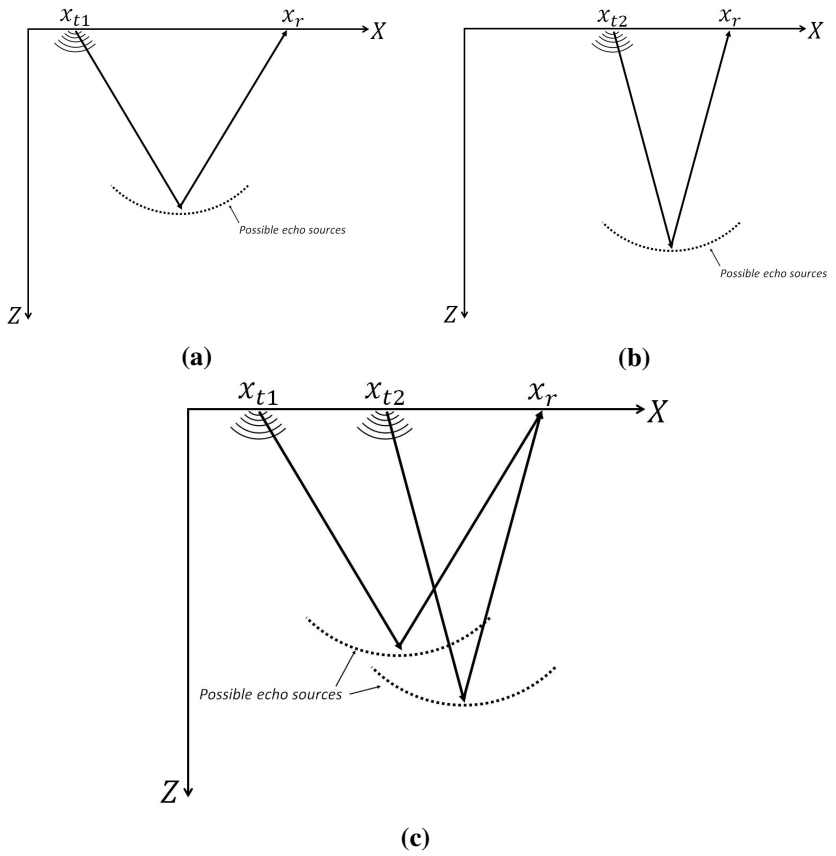

Figure 5.1: (a) Possible echo sources with transmission from x_{t1} received by x_r. (b) Possible echo sources with transmission from x_{t2} received by x_r. (c) Possible echo sources with simultaneous transmission from x_{t1} and x_{t2} received by x_r.

5.2 Previous Research

Spatial encoding was originally proposed to combat the inherently low SNR of SA imaging by transmitting with multiple elements simultaneously to increase the total acoustic energy entering the tissue. In [4] and [25] the authors suggest a Hadamard encoding scheme, where excitation pulse waveforms on each element transmitting simultaneously is multiplied by a column of a Hadamard encoding matrix. However, this design has the requirement that as many transmit events must be fired as there are simultaneous transmitters before the received RF can be

decoded, e.g., if 4 elements are set to fire simultaneously, they must do so 4 times before decoding. While this accomplishes the task of increasing the total acoustic energy entering the tissue in the same amount of time without losing resolution, it does not offer any advantage in higher frame rates. In [3], Chiao and Thomas suggest using orthogonal Golay codes in place of Hadamard codes, but this method faces the same drawback of requiring as many transmissions as active simultaneous transmitting elements.

An alternate approach to encoding was proposed by Gran and Jensen in [7], who expanded on the topic in [10]. In a typical ultrasound transducer, elements have an available frequency range in which they can transmit (e.g., the Ultrasonix L14-5 linear probe has a frequency range of 5 - 14 MHz [44]). Gran and Jensen separated this available bandwidth into disjoint subbands, each of which was assigned to one element of a simultaneously transmitting set. Received RF signals were isolated using simple frequency filters, determining which element the signal originated from. To gather information from the full possible frequency bandwidth of a given element, however, multiple transmits at different subbands had to be conducted to synthesize the full spectrum. Therefore, this approach also did not result in a net frame rate increase.

In 2008, Gran and Jensen proposed a spatial encoding technique with the main purpose of reducing the total number of transmission events required to form a full ultrasound image, achieved by devising an encoding technique that allows for decoding from a single transmission [9]. This paper was based on their previous research ([8, 11]), where pseudo-random encoding sequences are proposed. Section 5.3 presents an summary of the technique, as it is the essential basis for the original work presented later in this chapter. Greater detail can be found in [9].

5.3 Spatial Encoding with Code Division

This section is an overview of the key points of Gran and Jensen's paper [9], where full details can be found.

A single ultrasound transmit event with K simultaneous transmitting elements and Q receiving elements can be modeled, assuming that the system is fully linear, as

$$y_q^k(t) = \left\{ \sum_{p=1}^{P} s_p(\vec{r}_p) h_e(\vec{r}_k, \vec{r}_p, t) * h_r(\vec{r}_p, \vec{r}_q, t) \right\} * x_k(t), \tag{5.3}$$

where P is the number of scatterers in the medium (possibly infinite in tissue) and $s_p(\vec{r}_p)$ is the strength of the p^{th} scatterer. $h_e(\vec{r}_k, \vec{r}_p, t)$ is the spatial impulse response from the k^{th} transmitting element to the p^{th} scatterer, $*$ denotes convolution in the time domain, and $h_r(\vec{r}_p, \vec{r}_q, t)$ is the spatial impulse response from the p^{th} scatterer to the q^{th} receiving element. $\vec{r}_p$ is the position of the p^{th} scatterer, $\vec{r}_k$ is the position of the k^{th} transmitting element, and $\vec{r}_q$ is the position of the q^{th} receiving element. $x_k(t)$ is the code sequence transmitted by the k^{th} transmitting element. Because the spatial impulse response represents the entire transformation of the acoustic wave, including attenuation and the electromechanical transfer function of the transducer elements, a scattering function for an acoustic wave from the k^{th} transmitting element to the q^{th} receiving element can be written

$$h_{kq}(t) = \sum_{p=1}^{P} s_p(\vec{r}_p) h_e(\vec{r}_k, \vec{r}_p, t) * h_r(\vec{r}_p, \vec{r}_q, t). \tag{5.4}$$

For the total received signal at the q^{th} receiving element, Equation 5.3 can be combined into

$$y_q(t) = \sum_{k=1}^{K} h_{kq}(t) * x_k(t). \tag{5.5}$$

After passing through the ADC, and considering $v_q(n)$ to be the digitized noise process from the q^{th} (assumed Gaussian distribution with zero mean), Equation 5.5 becomes

$$y_q(n) = \sum_{k=1}^{K} h_{kq}(n) * x_k(n) + v_q(n), \tag{5.6}$$

where $h_{kq}(n)$ and $x_k(n)$ (with N samples) are the digitized versions of the scattering function $h_{kq}(t)$ and code sequence $x_k(t)$, respectively. Because the acoustic wave will decay as it travels through the medium, it can be modeled as a finite impulse response (FIR) process, where the transfer function of the digitized version the scattering function Equation 5.4 can be written as

$$H_{kq}(z^{-1}) = \sum_{m=0}^{M-1} h_{kq}(m) z^{-m}, \tag{5.7}$$

where M is the length of the impulse responses and z^{-1} is the unit backward-shift operator. Therefore, the output at the q^{th} receiving element becomes

$$y_q(n) = \sum_{k=1}^{K} \sum_{m=0}^{M-1} h_{kq}(m) x_k(n-m) + v_q(n). \tag{5.8}$$

$y_q(n)$ and $h_{kq}(n)$ are now written as column vectors

$$\mathbf{y}_q = \begin{pmatrix} y_q(0) & y_q(1) & \cdots & y_q(N+M-2) \end{pmatrix}^T \tag{5.9}$$

$$\mathbf{h}_{kq} = \begin{pmatrix} h_{kq}(0) & h_{kq}(1) & \cdots & h_{kq}(M-1) \end{pmatrix}^T \tag{5.10}$$

so the convolution between the waveform transmitted by the k^{th} element and the scattering function can be written as

$$\mathbf{y}_q = \sum_{k=1}^{K} \mathbf{X}_k \mathbf{h}_{kq} + \mathbf{v}_q, \tag{5.11}$$

where

$$\mathbf{X}_k = \begin{pmatrix} x_k(0) & 0 & \cdots & 0 \\ x_k(1) & x_k(0) & \ddots & 0 \\ \vdots & \ddots & \ddots & \vdots \\ x_k(N-1) & \ddots & \ddots & x_k(0) \\ 0 & x_k(N-1) & \ddots & x_k(1) \\ \vdots & \ddots & \ddots & \vdots \\ 0 & 0 & \cdots & x_k(N-1) \end{pmatrix} \tag{5.12}$$

with dimensions $(M+N) \times M$ and $\mathbf{v}_q$ is a zero mean noise process with Gaussian probability distribution and autocovariance matrix

$$E[\mathbf{v}_q \mathbf{v}_q^T] = \mathbf{Q}_v. \tag{5.13}$$

The signal matricies $\mathbf{X}_k$ of the k transmitting elements can be grouped to write a more compact version of Equation 5.11

$$\mathbf{y}_q = \underbrace{\begin{pmatrix}\mathbf{X}_1 & \mathbf{X}_2 & \cdots & \mathbf{X}_K\end{pmatrix}}_{\mathbf{X}} \underbrace{\begin{pmatrix}\mathbf{h}_{1q}\\ \mathbf{h}_{2q}\\ \vdots\\ \mathbf{h}_{Kq}\end{pmatrix}}_{h_q} + \mathbf{v}_q. \tag{5.14}$$

To find the most likely estimate of the scattering function vector $\mathbf{h}_q$, which can be used to generate the final image, the probability distribution of receiving output $\mathbf{y}$ given a set of scattering functions must first be calculated. This distribution is given by

$$p_{\mathbf{y}_q|h_q}(\mathbf{y}_q|\mathbf{h}_q) = \frac{1}{\sqrt{(2\pi)^{N+M-1}\det(\mathbf{Q}_v)}} \times \exp\left(-\frac{1}{2}(\mathbf{y}_q - \mathbf{X}\mathbf{h}_q)^T \mathbf{Q}_v^{-1}(\mathbf{y}_q - \mathbf{X}\mathbf{h}_q)\right) \tag{5.15}$$

as the only stochastic part of the scattering function is the noise, which is assumed to be Gaussian distributed. The scattering functions $\mathbf{h}_q$ that maximize Equation 5.15 must now be found, such that

$$\hat{\mathbf{h}}_q = \arg\max_{\mathbf{h}_q} p_{\mathbf{y}_q|\mathbf{h}_q}(\mathbf{y}_q|\mathbf{h}_q). \tag{5.16}$$

The solution to this optimization problem is taken from [21]:

$$\left(\mathbf{X}^T\mathbf{Q}_v^{-1}\mathbf{X}\right)\hat{\mathbf{h}}_q = \mathbf{X}^T\mathbf{Q}_v^{-1}\mathbf{y}_q \tag{5.17}$$

which, when considering that the noise process is white with variance σ_v^2 (i.e., $\mathbf{Q}_v = \sigma_v^2\mathbf{I}$), becomes

$$\left(\mathbf{X}^T\mathbf{X}\right)\hat{\mathbf{h}}_q = \mathbf{X}^T\mathbf{y}_q. \tag{5.18}$$

Assuming that $\mathbf{X}$ is full-rank, i.e., we select a code $x_k(n)$ of length N such that

$$N \geq (K-1)M + 1, \tag{5.19}$$

then the maximum likelihood estimate of $\mathbf{h}_q$ can be found:

$$\hat{\mathbf{h}}_q = \left(\mathbf{X}^T\mathbf{X}\right)^{-1}\mathbf{X}^T\mathbf{y}_q. \tag{5.20}$$

Because

$$\mathbf{h}_q = \begin{pmatrix} h_{1q} & h_{2q} & \cdots & h_{Kq} \end{pmatrix}^T, \tag{5.21}$$

as seen in Equation 5.14, $\hat{\mathbf{h}}_{kq}$ can be isolated for every value k. Since $\hat{\mathbf{h}}_{kq}$ represents an estimate of the signal that would have been received by the q^{th} receiving element had it transmitted alone and without a code, it can now be used for receive beamforming and image generation. Beamforming is conducted in the same SA method described in Section 2.1.5, but with a different value for τ (defined in Equation 5.28).

Gran and Jensen's work in this field, while achieving acceptable results in resolution and SNR, causes a significant drawback. For the received RF to be decodable, i.e., matrix $\mathbf{X}$ must be full-rank, Equation 5.19 must be observed. This means that for a region of interest M samples deep, a code length N of $(K-1)M+1$ samples must be transmitted into the tissue. Commercially available ultrasound imaging systems are limited by the half-duplex constraint, meaning that no elements can receive RF signals while any other element is transmitting. For a transmit sequence of N samples, then, the first N samples that would have been received by the receiving elements are lost. Therefore, the first N samples of the medium cannot be imaged. Furthermore, that region must also be completely void of scatters so as not to introduce artifacts into the received RF vector $\mathbf{y}_q$. For example, a medium to be imaged 5cm deep with two simultaneously active transmitting elements must have a 5cm empty area between it and the transducer. Although this fact is not specifically stated in Gran and Jensen's paper [9], the effect can be seen in Figure 4 of that paper where an imaging region of 2cm begins at 2.5cm, so there is 2.5cm of void space above the imaging region. In this chapter, the void space region is known as the "deadzone". To utilize Gran and Jensen's technique on a medium that does not have a natural deadzone like their test medium does, a device known as a standoff pad could be used (Figure 5.2). A standoff pad is an acoustically transparent device that sits between the transducer and the medium surface, thereby creating an empty

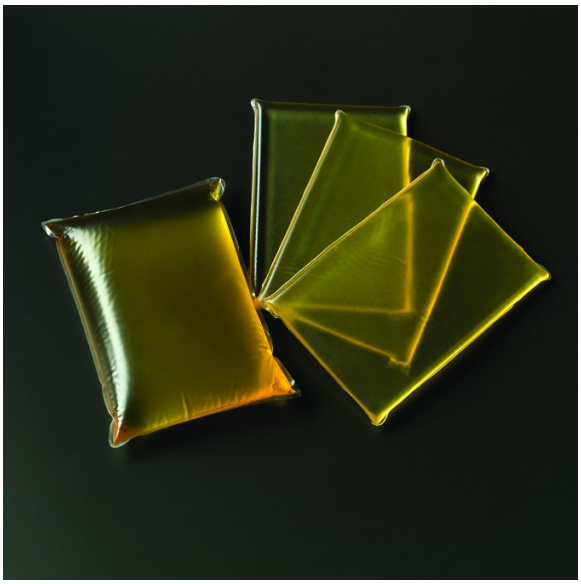

Figure 5.2: Reusable acoustic standoff pads. Image courtesy of CIVCO Medical Solutions.

area above the image. As ultrasound image quality decreases with depth, however, the requirement for a standoff pad that adds depth leads to images of poorer overall quality than those without standoffs.

5.4 Compressed Sensing

The original work presented in this chapter was completed as an extension of the spatial encoding method described in Section 5.3. To reduce and possibly remove the restriction of a deadzone, an alternate decoding scheme is proposed.

Many diagnostic and surgical procedures that require ultrasound imaging, such as intra-spinal needle guidance, generate RF data with a small set of very bright points in an otherwise dark region. In the intra-spinal needle guidance example, the needle and spine outline would generate extremely powerful reflections in comparison to the surrounding soft tissue (the acoustic wave does not effectively penetrate bone, and so only the spine outline would show). In such a scenario it can be assumed that the received RF is relatively sparse, where the soft tissue reflections are

near-zero in comparison to the bone and needle reflections.

Because of the sparsity of the received RF vector, an alternative decoding method known as "compressed sensing" can be used. Compressed sensing, as a general signal processing term, refers to the reconstruction of a signal by solving an underdetermined linear system by taking advantage of sparsity or compressibility in the system. This is done by formulating the decoding as a convex optimization problem, which can then be solved using a number of open-source or commercial programming toolboxes. The capability to solve an underdetermined linear system means that the code matrix $\mathbf{X}$ in Equation 5.20 no longer needs to be full-rank to estimate a solution, and therefore Equation 5.19 no longer needs to hold true. Removing that restriction on the code length N reduces the required depth of the deadzone, thereby removing the requirement for a standoff pad and bringing the medium closer to the transducer surface for an improvement in quality. In the following sections, experiments and results are described where the "compression ratio", i.e., the ratio of M imaged samples to N code samples for a 2-element simultaneous transmit, is reduced from < 1 requirement described in Equation 5.19 to as high as 5.

As a further extension, a technique titled "partial decoding" is presented in Section 5.5.2 where the half-duplex constraint is entirely removed by expanding the dimensions of code matrix $\mathbf{X}$ to estimate the medium's spatial impulse response h_{kq} from the tail end of the code that is received immediately after transmission ceases.

5.5 Experimental Design

An initial experiment was designed to replicate the results of the paper published by Gran and Jensen [9], described in Section 5.3. A Field II (Section 3.3) simulation was created using the same parameters for the transducer and ultrasound system: 7 MHz linear array with 0.208mm pitch, 0.035mm kerf, 4.5mm element height, 128 elements divided into groups of two for transmit with single elements on receive, and a 120 MHz ADC sampling rate. The element excitation pulse, however, was set as a single Dirac impulse instead of a sinusoid; this was changed to more accurately emulate the capabilities of a commercial ultrasound machine, which cannot transmit with variable power within a given excitation code.

40 sets of simulations were run with varying parameters. 20 sets were run on each of two phantoms, the first with six point scatters vertically spaced 5mm apart ("point phantom", similar to that used for simulations in [9] but with 2 extra point scatterers) and the second with six occlusions (three high-reflectivity and three low-reflectivity) set in a homogeneous tissue below skin and fat layers ("tissue phantom"), represented with 200,000 individual point scatterers. On each phantom, simulation sets were run for every combination of compression ratios of 0.9, 1, 3, and 5 and standoff pads of thickness 2 mm, 5 mm, 15 mm, 30 mm, and 50 mm. Each set consisted of the following:

1. "reference" simulation, where all transmit groups fired individually and without a coded excitation to simulate what conventional non-coded SA imaging would produce.

2. "Gran decoded" simulation, where two transmit groups fired simultaneously and the received RF was decoded using the method in Section 5.3.

3. "compressed decoded" simulation, where two transmit groups fired simultaneously and the received RF was decoded using a compressed sensing algorithm.

4. "compressed partial decoded" simulation, with the same transmit sequence and decoding as "compressed decoded" but with the code matrix $\mathbf{X}$ extended to estimate impulse responses from scatters in the deadzone by using only the tail of the received echo.

For the simulations that used coding (items 2, 3, and 4) 18-bit codes the same as in [9] was used:

$$x_1 = \begin{pmatrix} 1 & -1 & -1 & -1 & -1 & -1 & -1 & -1 & 1 & 1 & -1 & 1 & 1 & 1 & -1 & -1 & -1 & 1 \end{pmatrix} \tag{5.22}$$

$$x_2 = \begin{pmatrix} 1 & 1 & -1 & -1 & -1 & -1 & 1 & -1 & 1 & 1 & 1 & 1 & 1 & 1 & -1 & 1 & 1 & 1 \end{pmatrix}, \tag{5.23}$$

which were then oversampled to create a sparse code of length N. In [9] this oversampled code was then convolved with a sinusoidal excitation wave, but as the

excitation in this experiment was set as a Dirac impulse to emulate the capabilities of a physical ultrasound machine the convolution resulted in no change.

Simulations were run on a computer with dual Intel X5650 processors at 2.67 GHz and 24 GB random access memory running Windows 7 and using Matlab R2012b. Each simulation returned a set of received RF vectors $\mathbf{h}_q$ for every element q for each of the transmit groups in the reference simulation (item 1, independent transmits, no coding), and a set of received RF vectors $\mathbf{y}_q$ for every receiving element q for each of the transmit group pairs in the coded simulations (items 2, 3, and 4, two groups transmitting simultaneously). To find the vectors $\hat{\mathbf{h}}_q$ for item 2 (Gran decoded), the vectors $\mathbf{y}$ were decoded using the process described in Section 5.3.

5.5.1 Compressed Sensing

To find the vectors $\hat{\mathbf{h}}_q$ for item 3 (compressed decoded), $\mathbf{y}_q$ was decoded by formulating the system as a convex optimization problem and solving using the SDPT3 solver [41] in the CVX modeling system for Matlab [12, 13]. In theory, the objective of this problem would be to find the value for $\mathbf{h}_q$ such that

$$\hat{\mathbf{h}}_q = \arg\min_{\mathbf{h}_q} \|\mathbf{h}_q\|_0 \text{ s.t. } \mathbf{y}_q = \mathbf{X}\mathbf{h}_q. \tag{5.24}$$

In the presence of noise, this is revised to be

$$\hat{\mathbf{h}}_q = \arg\min_{\mathbf{h}_q} \|\mathbf{h}_q\|_0 \text{ s.t. } \|\mathbf{y}_q - \mathbf{X}\mathbf{h}_q\|_2 < \varepsilon, \tag{5.25}$$

where ε is a user-definable error value dependent on the expected noise level of the system [42]. Using the 0-norm, however, this problem is NP-hard. To reduce it to a quadratic problem, we relax it using the 1-norm as an approximation. The problem then becomes

$$\hat{\mathbf{h}}_q = \arg\min_{\mathbf{h}_q} \|\mathbf{h}_q\|_1 \text{ s.t. } \|\mathbf{y}_q - \mathbf{X}\mathbf{h}_q\|_2 < \varepsilon, \tag{5.26}$$

which is then solved using the CVX library. In these experiments, the value of ε was determined by imaging the tissue phantom with conventional SA imaging (all transmit events are independent) and taking the average response value within one

of the occlusions that, in theory, should be entirely zero values.

5.5.2 Compressed Sensing with Partial Decoding

To find the vectors $\mathbf{h}_q$ for item 4 (compressed partial decoded), the same processed was used as in Section 5.5.1 but with an extended code matrix $\mathbf{X}$. Instead of that presented in Equation 5.12, the code matrix was defined as

$$\mathbf{X}_k = \begin{pmatrix} x_k(N-1) & x_k(N-2) & \cdots & x_k(1) & x_k(0) & 0 & \cdots & 0 \\ 0 & x_k(N-1) & \ddots & x_k(2) & x_k(1) & x_k(0) & \ddots & 0 \\ \vdots & 0 & \ddots & \vdots & \vdots & \ddots & \ddots & \vdots \\ \vdots & \vdots & \ddots & x_k(N-1) & \vdots & \ddots & \ddots & x_k(0) \\ \vdots & \vdots & \ddots & 0 & x_k(N-1) & \ddots & \ddots & x_k(1) \\ \vdots & \vdots & \ddots & \vdots & 0 & x_k(N-1) & \ddots & \vdots \\ \vdots & \vdots & \ddots & \vdots & \vdots & \ddots & \ddots & \vdots \\ 0 & 0 & \cdots & 0 & 0 & 0 & \cdots & x_k(N-1) \end{pmatrix} \tag{5.27}$$

with dimensions $(M+N) \times (M+N-1)$. When decoding with this matrix, the given $\mathbf{h}_{kq}$ is of length $M+N-1$, as opposed to length M in the Section 5.3 method. The extra $N-1$ samples represent the spatial impulse responses from scatterers within the deadzone. Although the estimated values for these scatters are less accurate than those outside of the deadzone (which can be solved using the full length code instead of a partial one), they nevertheless entirely remove the requirement for a standoff pad.

5.5.3 Receive Beamforming

After the vectors $\hat{\mathbf{h}_q}$ have been determined, they are then dynamically receive beamformed and combined to generate full frames. Beamforming is performed in the same way as described in Section 2.1.5, but with τ defined as

$$\tau(x_k, x_q, x, z) = \frac{\sqrt{z^2 + (x - x_k)^2}}{c} + \frac{\sqrt{z^2 + (x - x_q)^2}}{c} \tag{5.28}$$

for a scatterer at (x,z), where x_k is the lateral position of the transmitting element and x_q is the lateral position of the receiving element.

After the vectors $\hat{\mathbf{h}}_q$ have been beamformed independently for each separate transmit group, the resultant beamformed sets are then summed to create the final frame.

5.5.4 Image Generation

After full frames were compiled through receive beamforming, the RF data was converted into a human-viewable format. This was done through the following steps:

1. Envelope detection: the envelope of the receive beamformed RF data was found by taking the absolute value of the Hilbert transform [30] of each column in the frame.

2. Logarithmic compression: to display greater detail in regions of low-power reflections, the image is logarimically compressed with a 50 dB dynamic range.

3. Interpolation: as the frame is much higher resolution vertically (thousands of samples) than horizontally (128 elements), the image is interpolated in the horizontal direction by a factor of 10.

4. The final data is scaled to provide an image that is the width of the transducer wide and as deep as the region that was imaged.

5.6 Results

The resulting images from each of the 20 simulation sets on the point phantom, shown in Appendix A, were compared according to their resolution. The images from each of the 20 simulation sets on the tissue phantom, shown in Appendix B, were compared according to their SNR at the occlusions.

5.6.1 Resolution

The lateral and axial resolution of each of the four techniques in Section 5.5 in each of the 20 simulation sets were measured at the full width at half maximum on the point spread response from the point scatterers. This is defined as the distance between the points on each side of the scatterer that are half the value of the highest value for that scatterer. These resolutions are presented in the tables Table 5.1 through Table 5.4. For point scatterers that were not visible, not detectable in the noise, or not fully defined, the resolution has been denoted as 'N/A'.

5.6.2 Signal-to-Noise Ratio

The SNR of each technique was measured by comparing the values inside an occlusion to the values outside the occlusion, according to the equation

$$SNR(dB) = 10\log_{10}\frac{|\mu_{in} - \mu_{out}|}{\sqrt{\sigma_{in}\sigma_{out}}}, \tag{5.29}$$

where μ_{in} and σ_{in} are the mean value and standard deviation inside the occlusion, and μ_{out} and σ_{out} are the mean value and standard deviation in the area surrounding the occlusion. The "inner" region was defined as a 4 mm diameter circle centred on the occlusion's centre, while the "outer" region was defined as the area within a 8 mm wide square centered on the occlusion's centre (excluding the inner region). This function was applied to each of the six occlusions in the imaged region (three high reflectivity, three low reflectivity). The results are presented in Table 5.5 through Table 5.8.

Table 5.1: Lateral and Axial Width-Half-Max (mm) of Point Spread Response for Compression Ratio of 0.9

Standoff Pad (mm)	Scatterer Depth (mm)	Reference		Gran Decoded		Compressed Decoded		Compressed Partial Decoded	
		Lateral	Axial	Lateral	Axial	Lateral	Axial	Lateral	Axial
2 (Figure A.1)	2	1.226	0.430	N/A	N/A	N/A	N/A	N/A	N/A
	7	0.997	0.423	N/A	N/A	N/A	N/A	N/A	N/A
	12	0.893	0.423	N/A	N/A	N/A	N/A	0.914	0.423
	17	0.893	0.417	N/A	N/A	N/A	N/A	0.956	0.417
	22	0.893	0.423	2.223	1.617	N/A	N/A	0.914	0.423
	27	0.872	0.423	2.389	0.648	N/A	N/A	0.872	0.423
5 (Figure A.2)	5	0.893	0.417	N/A	N/A	N/A	N/A	N/A	N/A
	10	0.872	0.417	N/A	N/A	N/A	N/A	0.872	0.417
	15	0.893	0.423	N/A	N/A	N/A	N/A	N/A	N/A
	20	0.914	0.423	N/A	N/A	N/A	N/A	0.914	0.423
	25	0.872	0.423	1.641	0.732	N/A	N/A	0.872	0.423
	30	0.893	0.423	1.226	0.892	N/A	N/A	0.893	0.423
15 (Figure A.3)	15	0.893	0.423	N/A	N/A	N/A	N/A	0.893	0.423
	20	0.914	0.423	N/A	N/A	N/A	N/A	0.914	0.423
	25	0.872	0.423	0.914	0.423	N/A	N/A	0.872	0.423
	30	0.893	0.423	0.935	0.449	N/A	N/A	0.893	0.423
	35	0.893	0.430	2.555	0.475	N/A	N/A	0.893	0.430
	40	0.893	0.423	0.893	0.622	N/A	N/A	0.893	0.423
30 (Figure A.4)	30	0.893	0.423	N/A	N/A	N/A	N/A	0.893	0.423
	35	0.893	0.430	N/A	N/A	N/A	N/A	0.893	0.430
	40	0.893	0.423	0.914	0.423	N/A	N/A	0.893	0.423
	45	0.852	0.423	0.872	0.423	N/A	N/A	0.852	0.423
	50	0.872	0.423	0.893	0.545	N/A	N/A	0.872	0.423
	55	0.914	0.423	0.997	0.475	N/A	N/A	0.914	0.423
50 (Figure A.5)	50	0.872	0.423	0.893	0.423	0.893	0.423	0.872	0.423
	55	0.914	0.423	0.914	0.423	0.914	0.423	0.914	0.423
	60	1.039	0.417	1.039	0.417	1.039	0.417	1.039	0.417
	65	1.080	0.417	1.122	0.417	1.122	0.417	1.080	0.417
	70	1.163	0.411	1.163	0.411	1.163	0.411	1.163	0.411
	75	1.205	0.411	1.205	0.411	1.205	0.411	1.205	0.411

Table 5.2: Lateral and Axial Width-Half-Max (mm) of Point Spread Response for Compression Ratio of 1

Standoff Pad (mm)	Scatterer Depth (mm)	Reference		Gran Decoded		Compressed Decoded		Compressed Partial Decoded	
		Lateral	Axial	Lateral	Axial	Lateral	Axial	Lateral	Axial
2 (Figure A.6)	2	1.226	0.430	N/A	N/A	N/A	N/A	N/A	N/A
	7	0.997	0.423	N/A	N/A	N/A	N/A	N/A	N/A
	12	0.893	0.423	N/A	N/A	N/A	N/A	N/A	N/A
	17	0.893	0.417	N/A	N/A	N/A	N/A	0.935	0.423
	22	0.893	0.423	N/A	N/A	N/A	N/A	0.914	0.423
	27	0.872	0.423	N/A	N/A	N/A	N/A	0.893	0.423
5 (Figure A.7)	5	0.893	0.417	N/A	N/A	N/A	N/A	N/A	N/A
	10	0.872	0.417	N/A	N/A	N/A	N/A	0.872	0.417
	15	0.893	0.423	N/A	N/A	N/A	N/A	0.893	0.423
	20	0.914	0.423	N/A	N/A	N/A	N/A	0.914	0.423
	25	0.872	0.423	N/A	N/A	N/A	N/A	0.872	0.423
	30	0.893	0.423	N/A	N/A	N/A	N/A	0.893	0.423
15 (Figure A.8)	15	0.893	0.423	N/A	N/A	N/A	N/A	0.893	0.423
	20	0.914	0.423	N/A	N/A	N/A	N/A	0.914	0.423
	25	0.872	0.423	N/A	N/A	N/A	N/A	0.872	0.423
	30	0.893	0.423	1.496	0.507	N/A	N/A	0.893	0.423
	35	0.893	0.430	N/A	N/A	N/A	N/A	0.893	0.430
	40	0.893	0.423	1.143	0.622	N/A	N/A	0.893	0.423
30 (Figure A.9)	30	0.893	0.423	N/A	N/A	N/A	N/A	0.893	0.423
	35	0.893	0.430	1.641	0.520	N/A	N/A	0.893	0.430
	40	0.893	0.423	N/A	N/A	N/A	N/A	0.893	0.423
	45	0.852	0.423	0.872	0.648	N/A	N/A	0.852	0.423
	50	0.872	0.423	0.872	0.430	N/A	N/A	0.872	0.423
	55	0.914	0.423	0.914	0.423	N/A	N/A	0.914	0.423
50 (Figure A.10)	50	0.872	0.423	0.893	0.423	0.893	0.423	0.872	0.423
	55	0.914	0.423	0.914	0.423	0.914	0.423	0.914	0.423
	60	1.039	0.417	1.080	0.417	1.039	0.417	1.039	0.417
	65	1.080	0.417	1.143	0.423	1.122	0.417	1.080	0.417
	70	1.163	0.411	1.163	0.411	1.163	0.411	1.163	0.411
	75	1.205	0.411	1.205	0.411	1.205	0.411	1.205	0.411

Table 5.3: Lateral and Axial Width-Half-Max (mm) of Point Spread Response for Compression Ratio of 3

Standoff Pad (mm)	Scatterer Depth (mm)	Reference		Gran Decoded		Compressed Decoded		Compressed Partial Decoded	
		Lateral	Axial	Lateral	Axial	Lateral	Axial	Lateral	Axial
2 (Figure A.11)	2	1.226	0.430	N/A	N/A	N/A	N/A	N/A	N/A
	7	0.997	0.423	N/A	N/A	N/A	N/A	N/A	N/A
	12	0.893	0.423	N/A	N/A	N/A	N/A	0.893	0.423
	17	0.893	0.417	N/A	N/A	N/A	N/A	0.893	0.417
	22	0.893	0.423	N/A	N/A	N/A	N/A	0.893	0.423
	27	0.872	0.423	N/A	N/A	N/A	N/A	0.872	0.423
5 (Figure A.12)	5	0.893	0.417	N/A	N/A	N/A	N/A	0.893	0.417
	10	0.872	0.417	N/A	N/A	N/A	N/A	0.872	0.417
	15	0.893	0.423	N/A	N/A	N/A	N/A	0.893	0.423
	20	0.914	0.423	N/A	N/A	N/A	N/A	0.914	0.423
	25	0.872	0.423	N/A	N/A	N/A	N/A	0.872	0.423
	30	0.893	0.423	N/A	N/A	N/A	N/A	0.893	0.423
15 (Figure A.13)	15	0.893	0.423	N/A	N/A	0.893	0.423	0.893	0.423
	20	0.914	0.423	N/A	N/A	0.914	0.423	0.914	0.423
	25	0.872	0.423	N/A	N/A	0.893	0.423	0.872	0.423
	30	0.893	0.423	N/A	N/A	0.893	0.423	0.893	0.423
	35	0.893	0.430	N/A	N/A	0.893	0.430	0.893	0.430
	40	0.893	0.423	N/A	N/A	0.893	0.423	0.893	0.423
30 (Figure A.14)	30	0.893	0.423	N/A	N/A	0.893	0.423	0.893	0.423
	35	0.893	0.430	N/A	N/A	0.893	0.430	0.893	0.430
	40	0.893	0.423	N/A	N/A	0.893	0.423	0.893	0.423
	45	0.852	0.423	N/A	N/A	0.872	0.423	0.852	0.423
	50	0.872	0.423	N/A	N/A	0.872	0.423	0.872	0.423
	55	0.914	0.423	N/A	N/A	0.914	0.423	0.914	0.423
50 (Figure A.15)	50	0.872	0.423	N/A	N/A	0.893	0.423	0.872	0.423
	55	0.914	0.423	N/A	N/A	0.914	0.423	0.914	0.423
	60	1.039	0.417	N/A	N/A	1.039	0.417	1.039	0.417
	65	1.080	0.417	N/A	N/A	1.122	0.417	1.080	0.417
	70	1.163	0.411	N/A	N/A	1.163	0.411	1.163	0.411
	75	1.205	0.411	N/A	N/A	1.205	0.411	1.205	0.411

Table 5.4: Lateral and Axial Width-Half-Max (mm) of Point Spread Response for Compression Ratio of 5

Standoff Pad (mm)	Scatterer Depth (mm)	Reference		Gran Decoded		Compressed Decoded		Compressed Partial Decoded	
		Lateral	Axial	Lateral	Axial	Lateral	Axial	Lateral	Axial
2 (Figure A.16)	2	1.226	0.430	N/A	N/A	N/A	N/A	1.226	0.430
	7	0.997	0.423	N/A	N/A	N/A	N/A	0.997	0.423
	12	0.893	0.423	N/A	N/A	N/A	N/A	0.893	0.423
	17	0.893	0.417	N/A	N/A	N/A	N/A	0.893	0.417
	22	0.893	0.423	N/A	N/A	N/A	N/A	0.893	0.423
	27	0.872	0.423	N/A	N/A	N/A	N/A	0.872	0.423
5 (Figure A.17)	5	0.893	0.417	N/A	N/A	N/A	N/A	0.893	0.417
	10	0.872	0.417	N/A	N/A	N/A	N/A	0.872	0.417
	15	0.893	0.423	N/A	N/A	N/A	N/A	0.893	0.423
	20	0.914	0.423	N/A	N/A	N/A	N/A	0.914	0.423
	25	0.872	0.423	N/A	N/A	N/A	N/A	0.872	0.423
	30	0.893	0.423	N/A	N/A	N/A	N/A	0.893	0.423
15 (Figure A.18)	15	0.893	0.423	N/A	N/A	0.893	0.423	0.893	0.423
	20	0.914	0.423	N/A	N/A	0.914	0.423	0.914	0.423
	25	0.872	0.423	N/A	N/A	0.893	0.423	0.872	0.423
	30	0.893	0.423	N/A	N/A	0.893	0.423	0.893	0.423
	35	0.893	0.430	N/A	N/A	0.893	0.430	0.893	0.430
	40	0.893	0.423	N/A	N/A	0.893	0.423	0.893	0.423
30 (Figure A.19)	30	0.893	0.423	N/A	N/A	0.893	0.423	0.893	0.423
	35	0.893	0.430	N/A	N/A	0.893	0.430	0.893	0.430
	40	0.893	0.423	N/A	N/A	0.893	0.423	0.893	0.423
	45	0.852	0.423	N/A	N/A	0.872	0.423	0.852	0.423
	50	0.872	0.423	N/A	N/A	0.872	0.423	0.872	0.423
	55	0.914	0.423	N/A	N/A	0.914	0.423	0.914	0.423
50 (Figure A.20)	50	0.872	0.423	N/A	N/A	0.893	0.423	0.872	0.423
	55	0.914	0.423	N/A	N/A	0.914	0.423	0.914	0.423
	60	1.039	0.417	N/A	N/A	1.039	0.417	1.039	0.417
	65	1.080	0.417	N/A	N/A	1.122	0.417	1.080	0.417
	70	1.163	0.411	N/A	N/A	1.163	0.411	1.163	0.411
	75	1.205	0.411	N/A	N/A	1.205	0.411	1.205	0.411

Table 5.5: SNR (dB) of High and Low Reflectivity Occlusions for Compression Ratio of 0.9

Standoff Pad (mm)	Occlusion Depth (mm)	Reference		Gran Decoded		Compressed Decoded		Compressed Partial Decoded	
		High	Low	High	Low	High	Low	High	Low
2 (Figure B.1)	2	4.029	2.847	N/A	N/A	N/A	N/A	2.736	-5.312
	7	4.342	3.599	N/A	N/A	N/A	N/A	3.551	-5.430
	12	4.967	4.037	2.339	0.093	-0.501	0.548	4.629	1.227
5 (Figure B.2)	5	4.109	3.506	N/A	N/A	N/A	N/A	3.092	-7.705
	10	4.419	3.825	N/A	N/A	N/A	N/A	3.790	-0.369
	15	5.035	4.239	0.755	-4.716	-17.078	-4.903	4.894	1.889
15 (Figure B.3)	15	4.751	3.982	N/A	N/A	N/A	N/A	4.801	0.990
	20	4.710	3.808	2.408	-0.813	-1.509	-13.742	4.724	1.985
	25	5.138	4.391	1.137	-7.177	-12.450	-5.716	5.239	2.702
30 (Figure B.4)	30	4.811	4.044	1.991	-7.300	-5.081	-11.752	4.982	3.422
	35	4.839	3.747	1.422	-7.227	-7.892	-6.431	5.100	2.685
	40	5.291	4.328	1.165	-2.021	-4.068	-4.006	5.390	3.608
50 (Figure B.5)	50	4.887	4.094	4.889	4.103	4.889	4.103	5.123	3.664
	55	4.888	3.834	4.886	3.805	4.886	3.805	5.094	3.496
	60	5.390	4.094	5.390	4.073	5.390	4.073	5.493	3.822

Table 5.6: SNR (dB) of High and Low Reflectivity Occlusions for Compression Ratio of 1

Standoff Pad (mm)	Occlusion Depth (mm)	Reference		Gran Decoded		Compressed Decoded		Compressed Partial Decoded	
		High	Low	High	Low	High	Low	High	Low
2 (Figure B.6)	2	4.029	2.847	N/A	N/A	N/A	N/A	2.766	-5.241
	7	4.342	3.599	N/A	N/A	N/A	N/A	3.331	-6.303
	12	4.967	4.037	0.408	-2.533	-0.480	-2.543	4.717	1.659
5 (Figure B.7)	5	4.109	3.506	N/A	N/A	N/A	N/A	3.112	-14.005
	10	4.419	3.825	4.365	6.720	5.368	5.263	4.002	-1.640
	15	5.035	4.239	-1.641	-8.300	-9.005	-2.866	4.951	1.886
15 (Figure B.8)	15	4.751	3.982	N/A	N/A	N/A	N/A	4.678	0.984
	20	4.710	3.808	0.494	-1.897	-0.095	-0.655	4.610	2.108
	25	5.138	4.391	-2.123	-8.759	-14.070	-13.136	5.142	2.977
30 (Figure B.9)	30	4.811	4.044	-0.976	-4.864	-1.025	-5.013	5.019	3.112
	35	4.839	3.747	-1.765	-7.869	-1.783	-7.943	4.961	2.698
	40	5.291	4.328	-1.877	-1.225	-1.868	-1.238	5.423	3.630
50 (Figure B.10)	50	4.887	4.094	4.767	3.730	4.889	4.103	5.107	3.673
	55	4.888	3.834	4.686	3.735	4.887	3.803	5.031	3.291
	60	5.390	4.094	5.180	3.852	5.391	4.072	5.523	3.932

Table 5.7: SNR (dB) of High and Low Reflectivity Occlusions for Compression Ratio of 3

Standoff Pad (mm)	Occlusion Depth (mm)	Reference		Gran Decoded		Compressed Decoded		Compressed Partial Decoded	
		High	Low	High	Low	High	Low	High	Low
2 (Figure B.11)	2	4.029	2.847	-3.795	-20.825	-5.230	-6.264	3.400	-1.742
	7	4.342	3.599	-4.887	-13.745	-4.188	-10.720	3.909	0.701
	12	4.967	4.037	-4.561	-0.662	0.764	-11.192	4.682	1.271
5 (Figure B.12)	5	4.109	3.506	-5.756	-8.189	-2.553	-11.283	3.621	-0.940
	10	4.419	3.825	-4.431	-10.371	-2.721	-4.697	4.262	1.627
	15	5.035	4.239	-9.123	-17.546	2.294	-8.622	4.861	1.425
15 (Figure B.13)	15	4.751	3.982	-1.433	-8.257	4.915	2.539	4.628	1.564
	20	4.710	3.808	-8.311	-1.009	4.681	2.258	4.634	2.163
	25	5.138	4.391	-11.112	-5.151	5.146	2.757	5.119	2.547
30 (Figure B.14)	30	4.811	4.044	-4.740	-7.861	4.798	2.226	4.656	1.615
	35	4.839	3.747	-4.897	-19.505	5.079	1.775	5.074	1.863
	40	5.291	4.328	-0.722	-6.025	5.364	3.075	5.345	3.026
50 (Figure B.15)	50	4.887	4.094	-4.350	-11.268	5.040	2.465	4.968	1.851
	55	4.888	3.834	-1.455	-12.222	4.958	1.330	4.895	1.312
	60	5.390	4.094	-4.114	-8.792	5.333	2.990	5.313	2.977

Table 5.8: SNR (dB) of High and Low Reflectivity Occlusions for Compression Ratio of 5

Standoff Pad (mm)	Occlusion Depth (mm)	Reference		Gran Decoded		Compressed Decoded		Compressed Partial Decoded	
		High	Low	High	Low	High	Low	High	Low
2 (Figure B.16)	2	4.029	2.847	-6.809	-5.978	-4.780	-7.780	3.617	0.108
	7	4.342	3.599	-3.854	-7.240	-0.282	-10.124	3.886	1.410
	12	4.967	4.037	-9.262	-8.948	4.876	1.356	4.814	0.584
5 (Figure B.17)	5	4.109	3.506	-6.188	-7.338	-7.761	-5.791	3.635	0.800
	10	4.419	3.825	-12.921	-9.221	1.568	-0.595	4.025	0.977
	15	5.035	4.239	-6.007	-6.489	4.732	1.330	4.592	1.080
15 (Figure B.18)	15	4.751	3.982	-7.357	-4.022	4.375	0.763	4.243	0.735
	20	4.710	3.808	-16.305	-7.266	4.186	0.988	4.163	0.946
	25	5.138	4.391	-5.518	-6.040	4.804	1.270	4.794	1.209
30 (Figure B.19)	30	4.811	4.044	-4.268	-6.408	4.485	0.784	4.426	0.619
	35	4.839	3.747	-2.185	-16.081	4.504	0.805	4.487	0.822
	40	5.291	4.328	-6.225	-11.858	5.115	1.836	5.111	1.840
50 (Figure B.20)	50	4.887	4.094	1.325	-2.893	4.873	0.721	4.854	0.588
	55	4.888	3.834	-0.234	-8.125	4.941	1.174	4.935	1.156
	60	5.390	4.094	0.134	-4.737	5.356	2.409	5.359	2.418

5.7 Discussion

5.7.1 Gran Decoding

As stated Equation 5.19, for a two-element simultaneous transmit $N \geq M+1$ code matrix $\mathbf{X}$ to be full-rank. In the simulations, this value is modified as

$$N = \frac{M+1}{C}, \tag{5.30}$$

where C is the compression ratio. Due to the half-duplex constraint of elements being unable to receive while transmitting, this results in a deadzone of depth N samples. The effects of this deadzone can be seen in the simulation images and resolution/SNR results. For a compression ratio of 1 the deadzone will be roughly half the depth of the entire image. As seen by the 'N/A' results in Table 5.2 this will result in any scatterer within that region being undetectable, with the additional effect of scatterers below it being significantly distorted.

As the Gran Decoded method requires a full-rank code matrix to function, the results rapidly deteriorate as C is increased and the code matrix becomes underdetermined, even for points that were entirely outside the deadzone. This effect can be seen in Table 5.3 and Table 5.4, where the Gran decoding method was unable to distinguish a point scatterer at any depth.

5.7.2 Compressed Sensing Decoding

In simulations where scatterers fall within the deadzone, the compressed sensing decoding method is shown to perform worse than the Gran technique with significantly more distortion (Table 5.2 fourth row, Figure A.9). At higher compression ratios, however, the deadzone decreases in size and allows for a smaller standoff pad to be used (less void space required). For simulations at a compression ratio greater than 1 and with no scatterers within the deadzone, the compressed sensing method is shown to outperform the Gran decoding method in every case, with equal resolutions for scatterers detected by both methods and far more scatterers detected in general.

The resolution of this method is shown to be comparable to that of conven-

tional non-coded SA imaging for all cases with no scatterers in the deadzone (e.g., Table 5.4 rows 3-5). For high-reflectivity regions, the SNR is also comparable. It does, however, suffer from a significant drop in SNR for low-reflectivity occlusions in non-sparse media (the tissue phantom) at high compression ratios (e.g., Table 5.8, rows 3-5). This is a result of the required assumption for compressed sensing that the only points of interest are those with high reflectivity.

5.7.3 Compressed Sensing with Partial Decoding

This method shows a distinct advantage in scenarios where scatterers fall within the deadzone. In Table 5.4 (first row), it can be seen that the partial decoding method allows for detection of scatterers that neither the Gran decoding or basic compressed sensing decoding could, and at an equivalent resolution to that of the reference simulation. In Table 5.8 (rows 1-2) the partial decoding method also shows a drastic improvement in SNR over that of the Gran decoded and compressed decoded methods for both high- and low-reflectivity occlusions (although still significantly lower for low-reflectivity occlusions than the reference simulation).

5.7.4 Summary

The compressed sensing with partial decoding method shows to be superior to both Gran decoding and basic compressed sensing in all regards. It allows for detection of scatterers within the deadzone, as well as the best resolution and SNR of the three coded excitation methods. With 32 transmit events required for each of the simulations conducted, it offers an 8-fold increase in FPS over the default 256 transmit settings of a conventional ultrasound machine.

Although an improvement over other coded excitation methods, compressed sensing with partial decoding suffers from the drawback of poor SNR for low-reflectivity regions in non-sparse media. This is in line with the expectations described in Section 5.4, and shows promise for applications that require the reliable detection of only the high-reflectivity scatterers.

Chapter 6

Conclusions

High frame rate ultrasound imaging has the potential to allow for advanced imaging techniques at a exceptionally low cost and with no known patient risk. 3-D volumetric imaging, transient elastography, and fast Doppler sonography are several of the tools that would benefit most from a fully capable fast-imaging ultrasound technique. In addition, fast ultrasonography reduces motion blur when imaging quick-moving organs such as the heart.

One method for increasing ultrasound frame rate without loss of resolution or SNR has been proposed where the previously designed techniques of synthetic aperture (SA) and compounded plane wave (CPW) are adaptively combined to achieve an imaging method that integrates the benefit of each without the drawbacks. A second method has also been proposed where the work of Gran and Jensen [9] in spatial encoding is extended to vastly improve the applicability of the method and remove the limitations.

6.1 Thesis Contributions

- Synthetic aperture (SA) and compounded plane wave (CPW) techniques previously only performed in simulations or on dedicated research equipment were implemented on commercially available ultrasound equipment. The methods were performed using the SONIXRP and SONIXDAQ hardware from Ultrasonix Medical Corporation and using the Texo software development

kit for sequence control. This low-cost physical implementation allows for further research in the area with minimal difficulty and expense.

- An adaptive compounding technique was developed that combines the resolution of SA imaging with the SNR of CPW imaging. The technique allows for a higher frame rate than conventional fixed transmit beamforming imaging (double the frame rate in the experiments conducted) while maintaining an improvement in both axial and lateral resolution as well as SNR.

- An extension on the spatial encoding method developed in [9] was proposed and tested, which removes the full-rank requirement for the code matrix by implementing a compressed sensing technique. Reducing the rank of the code matrix allows for a reduction in the size of the deadzone produced by the half-duplex constraint on the transducer elements (cannot receive while transmitting). Experiments were conducted with a compression ratio (ratio of imaged samples to code length) ranging from 0.9 to 5, and showed a marked improvement over the Gran decoding technique [9] in all cases with a compression ratio greater than 1 where there were no scatterers located in the deadzone. This method is targeted for applications requiring detection of high-reflectivity scatterers only, as the SNR for low-reflectivity scatterers is poorer than that of conventional non-coded SA imaging.

- A further extension on the compressed sensing technique was proposed and tested, which extends the code matrix to allow for decoding of the tails of reflections originating in the deadzone (partial codes). This technique allows for imaging of scatterers within the deadzone, and eliminates the negative effect they have on scatterers below the deadzone. It shows an improvement over both the Gran decoding method and the basic compressed sensing method in lateral resolution, axial resolution, and SNR for both high- and low-reflectivity occlusions. The SNR for low-reflectivity occlusions at high compression ratios is poorer then that of non-coded SA imaging, and as such is targeted for applications requiring detection of high-reflectivity scatterers only.

6.2 Future Work

For the adaptive compounding method described in Chapter 4, future work will focus on testing the technique *in vivo* (on living tissue). Although the physical implementation on the Ultrasonix equipment is a large step towards clinical applications, the method may need to be modified to handle motion within the tissue during imaging. Future work may also focus on improving the adaptive weighting algorithm (Equation 4.5) to be more resilient to outliers in the strength of the RF data of the CPW image.

For the compressed sensing spatial encoding method described in Chapter 5, future work will focus primarily on implementing the technique on a physical ultrasound platform with quality assurance phantoms to determine its effectiveness outside of simulations. Eventually, that would be extended to tests on *in vivo* media. Currently, physical implementation is limited by the incapability of the Ultrasonix platforms to excite multiple elements simultaneously with individual excitation pulses, but that feature is expected to be available in the future. Additional work may focus on developing an application-specific convex optimization algorithm to improve the accuracy of the decoded result and the speed at which it is found.

Both techniques require a variety of user-definable parameters, including SA transmit aperture width, CPW angles, compression ratio, and excitation pulse shape/power. Although the selected values of these parameters are heavily dependent upon the medium being imaged, it may be possible to develop self-adjusting algorithms for determining their optimal values.

Due to hardware limitations and processing requirements, the proposed techniques in both Chapter 4 and Chapter 5 are currently only capable of being run in an offline mode, i.e., they cannot be run as real-time imaging. Future improvements in computer processing ability, coupled with implementation of data processing on a graphics processing unit (GPU) for massive multi-threading, will allow for real-time processing.

Bibliography

[1] J. Bercoff, S. Chaffai, M. Tanter, L. Sandrin, S. Catheline, M. Fink, J. Gennisson, and M. Meunier. In vivo breast tumor detection using transient elastography. *Ultrasound in Medicine & Biology*, 29(10):1387 – 1396, 2003. ISSN 0301-5629. doi:10.1016/S0301-5629(03)00978-5. URL http://www.sciencedirect.com/science/article/pii/S0301562903009785. 2, 11, 20

[2] C. Burckhardt, P.-A. Grandchamp, and H. Hoffmann. An experimental 2 mhz synthetic aperture sonar system intended for medical use. *Sonics and Ultrasonics, IEEE Transactions on*, 21(1):1 –6, Jan 1974. ISSN 0018-9537. doi:10.1109/T-SU.1974.29783. 10

[3] R. Chiao and L. Thomas. Synthetic transmit aperture imaging using orthogonal golay coded excitation. In *Ultrasonics Symposium, 2000 IEEE*, volume 2, pages 1677–1680 vol.2, 2000. doi:10.1109/ULTSYM.2000.921644. 20, 32

[4] R. Chiao, L. Thomas, and S. Silverstein. Sparse array imaging with spatially-encoded transmits. In *Ultrasonics Symposium, 1997. Proceedings., 1997 IEEE*, volume 2, pages 1679 –1682 vol.2, Oct 1997. doi:10.1109/ULTSYM.1997.663318. 20, 31

[5] J. Flaherty. Synthetic aperture ultrasonic imaging systems, 12 1970. 10

[6] K. Gammelmark and J. Jensen. Multielement synthetic transmit aperture imaging using temporal encoding. *Medical Imaging, IEEE Transactions on*, 22(4):552 –563, Apr 2003. ISSN 0278-0062. doi:10.1109/TMI.2003.809088. 20

[7] F. Gran and J. Jensen. Multi element synthetic aperture transmission using a frequency division approach. In *Ultrasonics, 2003 IEEE Symposium on*, volume 2, pages 1942–1946 Vol.2, 2003. doi:10.1109/ULTSYM.2003.1293297. 20, 32

[8] F. Gran and J. Jensen. Identification of pulse echo impulse responses for multi source transmission. In *Signals, Systems, and Computers, Thirty-Eighth Annular Asilomar Conference on*, pages 168–172, 2004. 32

[9] F. Gran and J. Jensen. Spatial encoding using a code division technique for fast ultrasound imaging. *Ultrasonics, Ferroelectrics and Frequency Control, IEEE Transactions on*, 55(1):12–23, 2008. ISSN 0885-3010. doi:10.1109/TUFFC.2008.613. 4, 32, 36, 38, 39, 54, 55

[10] F. Gran and J. A. Jensen. Spatio-temporal encoding using narrow-band linear frequency modulated signals in synthetic aperture ultrasound imaging. pages 405–416, 2005. doi:10.1117/12.592352. URL +http://dx.doi.org/10.1117/12.592352. 20, 32

[11] F. Gran, J. A. Jensen, and A. Jakobsson. A code division technique for multiple element synthetic aperture transmission. pages 300–306, 2004. doi:10.1117/12.535222. URL +http://dx.doi.org/10.1117/12.535222. 32

[12] M. Grant and S. Boyd. Graph implementations for nonsmooth convex programs. In V. Blondel, S. Boyd, and H. Kimura, editors, *Recent Advances in Learning and Control*, Lecture Notes in Control and Information Sciences, pages 95–110. Springer-Verlag Limited, 2008. http://stanford.edu/~boyd/graph_dcp.html. 40

[13] M. Grant and S. Boyd. CVX: Matlab software for disciplined convex programming, version 2.0 beta. http://cvxr.com/cvx, Sept. 2012. 40

[14] I. Holfort, A. Austeng, J.-F. Synnevg, S. Holm, F. Gran, and J. Jensen. Adaptive receive and transmit apodization for synthetic aperture ultrasound imaging. In *Ultrasonics Symposium (IUS), 2009 IEEE International*, pages 1 –4, sept. 2009. doi:10.1109/ULTSYM.2009.5442035. 10

[15] J. Jensen. Field ii simulation program. URL http://field-ii.dk. Accessed: 2013-07-29. 17

[16] J. Jensen. *Linear description of ultrasound imaging systems*. 1999. 18

[17] J. A. Jensen. Field: A program for simulating ultrasound systems. In *10TH NORDICBALTIC CONFERENCE ON BIOMEDICAL IMAGING, VOL. 4, SUPPLEMENT 1, PART 1:351–353*, pages 351–353, 1996. 17

[18] J. A. Jensen, S. I. Nikolov, K. L. Gammelmark, and M. H. Pedersen. Synthetic aperture ultrasound imaging. *Ultrasonics*, 44, Supplement(0):e5 –

e15, 2006. ISSN 0041-624X. doi:10.1016/j.ultras.2006.07.017. URL http://www.sciencedirect.com/science/article/pii/S0041624X06003374. Proceedings of Ultrasonics International (UI05) and World Congress on Ultrasonics (WCU). 9, 19

[19] M. Karaman, P.-C. Li, and M. O'Donnell. Synthetic aperture imaging for small scale systems. *Ultrasonics, Ferroelectrics and Frequency Control, IEEE Transactions on*, 42(3):429 –442, May 1995. ISSN 0885-3010. doi:10.1109/58.384453. 20, 22

[20] K. Kotowick, R. Rohling, and L. Lampe. Adaptive compounding of synthetic aperture and compounded plane-wave imaging for fast ultrasonography. In *Biomedical Imaging (ISBI), 2013 IEEE 10th International Symposium on*, pages 784–787, 2013. doi:10.1109/ISBI.2013.6556592. iii

[21] L. Ljung. *System Identification: Theory for the User*. Prentice-Hall, Englewood Cliffs, NJ, 1987. 35

[22] G. Lockwood and F. Foster. Design of sparse array imaging systems. In *Ultrasonics Symposium, 1995. Proceedings., 1995 IEEE*, volume 2, pages 1237 –1243 vol.2, Nov 1995. doi:10.1109/ULTSYM.1995.495782. 10

[23] G. Lockwood, J. Talman, and S. Brunke. Real-time 3-d ultrasound imaging using sparse synthetic aperture beamforming. *Ultrasonics, Ferroelectrics and Frequency Control, IEEE Transactions on*, 45(4):980 –988, Jul 1998. ISSN 0885-3010. doi:10.1109/58.710573. 10

[24] E. Mendelson, J.-F. Chen, and P. Karstaedt. Assessing tissue stiffness may boost breast imaging specificity. *Diagn. Imaging*, 31:15–17, 2009. 2

[25] T. X. Misaridis and J. A. Jensen. Spacetime encoding for high frame rate ultrasound imaging. *Ultrasonics*, 40(18):593 – 597, 2002. ISSN 0041-624X. doi:http://dx.doi.org/10.1016/S0041-624X(02)00179-8. URL http://www.sciencedirect.com/science/article/pii/S0041624X02001798. 20, 31

[26] G. Montaldo, M. Tanter, J. Bercoff, N. Benech, and M. Fink. Coherent plane-wave compounding for very high frame rate ultrasonography and transient elastography. *Ultrasonics, Ferroelectrics and Frequency Control, IEEE Transactions on*, 56(3):489 –506, Mar 2009. ISSN 0885-3010. doi:10.1109/TUFFC.2009.1067. 20

[27] K. Nagai. A new synthetic-aperture focusing method for ultrasonic b-scan imaging by the fourier transform. *Sonics and Ultrasonics, IEEE Transactions on*, 32(4):531 –536, Jul 1985. ISSN 0018-9537. doi:10.1109/T-SU.1985.31627. 10

[28] M. O'Donnell and L. Thomas. Efficient synthetic aperture imaging from a circular aperture with possible application to catheter-based imaging. *Ultrasonics, Ferroelectrics and Frequency Control, IEEE Transactions on*, 39(3):366 –380, May 1992. ISSN 0885-3010. doi:10.1109/58.143171. 10

[29] M. O'Donnell and Y. Wang. Coded excitation for synthetic aperture ultrasound imaging. *Ultrasonics, Ferroelectrics and Frequency Control, IEEE Transactions on*, 52(2):171 –176, Feb 2005. ISSN 0885-3010. doi:10.1109/TUFFC.2005.1406544. 20

[30] A. V. Oppenheim and R. W. Schafer. *Discrete-Time Signal Processing*. Prentice-Hall, NJ, 1989. 42

[31] J. rgen Arendt Jensen. A model for the propagation and scattering of ultrasound in tissue. *The Journal of the Acoustical Society of America*, 89 (1):182–190, 1991. doi:10.1121/1.400497. URL http://link.aip.org/link/?JAS/89/182/1. 17

[32] L. Sandrin, S. Catheline, M. Tanter, X. Hennequin, and M. Fink. Time-resolved pulsed elastography with ultrafast ultrasonic imaging. *Ultrasonic Imaging*, 21(4):259 –272, Dec 1999. 10, 20

[33] L. Sandrin, S. Catheline, M. Tanter, and M. Fink. 2d transient elastography. In M. Halliwell and P. N. T. Wells, editors, *Acoustical Imaging*, pages 485–492. Springer US, 2002. ISBN 978-0-306-47107-0. URL http://dx.doi.org/10.1007/0-306-47107-8_68. 10.1007/0-306-47107-8_68. 10, 20

[34] D. P. Shattuck and O. T. von Ramm. Compound scanning with a phased array. *Ultrasonic Imaging*, 4(2):93 – 107, 1982. ISSN 0161-7346. doi:http://dx.doi.org/10.1016/0161-7346(82)90094-3. URL http://www.sciencedirect.com/science/article/pii/0161734682900943. 6

[35] M. Soumekh. *Synthetic Aperture Radar Signal Processing with MATLAB Algorithms*. Wiley-Interscience publication. Wiley, 1999. ISBN 9780471297062. URL http://books.google.ca/books?id=gVWqQgAACAAJ. 9

[36] P. R. Stepanishen. Transient radiation from pistons in an infinite planar baffle. *The Journal of the Acoustical Society of America*, 49(5B): 1629–1638, 1971. doi:10.1121/1.1912541. URL http://link.aip.org/link/?JAS/49/1629/1. 17

[37] P. R. Stepanishen. The time-dependent force and radiation impedance on a piston in a rigid infinite planar baffle. *The Journal of the Acoustical Society of America*, 49(3B):841–849, 1971. doi:10.1121/1.1912424. URL http://link.aip.org/link/?JAS/49/841/1. 17

[38] P. R. Stepanishen. Pulsed transmit/receive response of ultrasonic piezoelectric transducers. *The Journal of the Acoustical Society of America*, 69(6):1815–1827, 1981. doi:10.1121/1.385919. URL http://link.aip.org/link/?JAS/69/1815/1. 17

[39] M. Tang, F. Luo, and D. Liu. Automatic time gain compensation in ultrasound imaging system. In *Bioinformatics and Biomedical Engineering , 2009. ICBBE 2009. 3rd International Conference on*, pages 1–4, 2009. doi:10.1109/ICBBE.2009.5162432. 8

[40] J. Taylor, J. Chan, and G. Thomas. Frequency selection for compounding synthetic aperture ultrasound images. In *Imaging Systems and Techniques (IST), 2012 IEEE International Conference on*, pages 74 –77, Jul 2012. doi:10.1109/IST.2012.6295514. 20

[41] K. C. Toh, M. Todd, and R. H. Ttnc. Sdpt3 – a matlab software package for semidefinite programming. *OPTIMIZATION METHODS AND SOFTWARE*, 11:545–581, 1999. 40

[42] J. Tropp and S. Wright. Computational methods for sparse solution of linear inverse problems. *Proceedings of the IEEE*, 98(6):948–958, 2010. ISSN 0018-9219. doi:10.1109/JPROC.2010.2044010. 40

[43] G. E. Tupholme. Generation of acoustic pulses by baffled plane pistons. *Mathematika*, 16, 1969. doi:10.1112/S0025579300008184. 17

[44] Ultrasonix Medical Corp. Transducer guide, . URL http://www.ultrasonix.com/webfm_send/879. Accessed: 2013-07-31. 32

[45] Ultrasonix Medical Corp. Sonix RP, . URL http://www.ultrasonix.com/wikisonix/index.php/Sonix_RP. Accessed: 2013-07-17. 13

[46] L. D. C. W. T. D. W. J. H. W. J. L. W. A. Anderson, J. T. Arnold and L. T. Zitelli. A new real-tim phased-array sector scanner for imaging the entire adult human heart. *Ultrasound in Medicine*, 3B:1547–1558, 1977. 6

Appendix A

Compressed Sensing Point Phantom Images

This appendix contains the resulting images from the 20 simulations conducted on the point phantom (Section 5.5) for each combination of compression ratios 0.9, 1, 3, 5 and standoff pad thicknesses of 2mm, 5mm, 15mm, 30mm, 50mm.

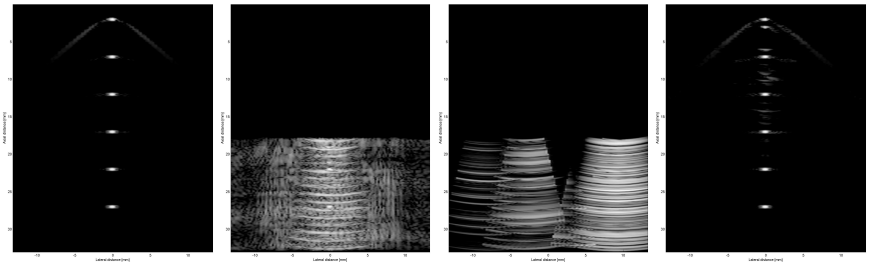

(a) **(b)** **(c)** **(d)**

Figure A.1: Point phantom simulation with compression ratio of 0.9 and standoff pad thickness of 2 mm. (a) Reference simulation. (b) Gran Decoded. (c) Compressed Sensing Decoded. (d) Compressed Sensing Partial Decoded.

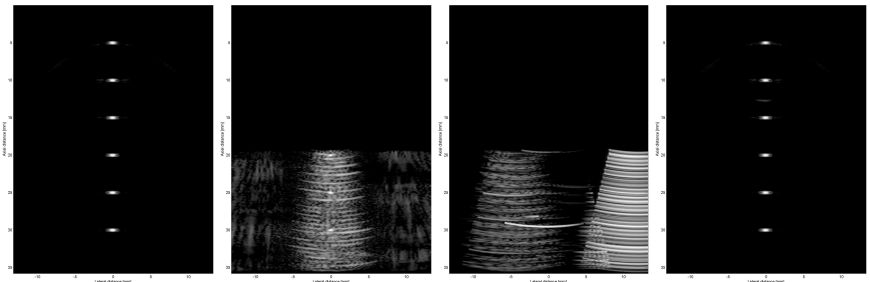

(a) **(b)** **(c)** **(d)**

Figure A.2: Point phantom simulation with compression ratio of 0.9 and standoff pad thickness of 5 mm. (a) Reference simulation. (b) Gran Decoded. (c) Compressed Sensing Decoded. (d) Compressed Sensing Partial Decoded.

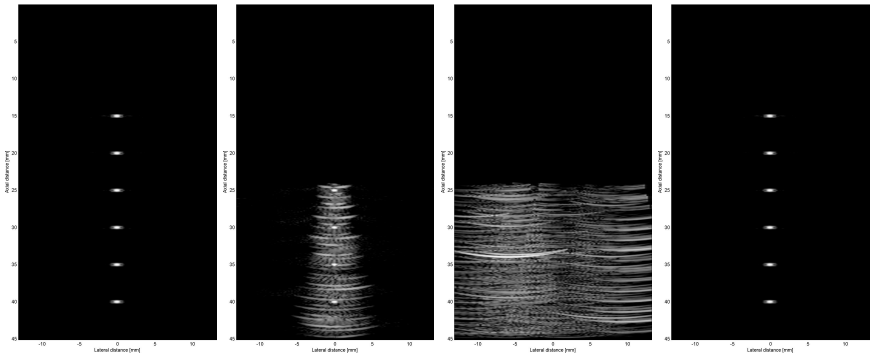

(a) **(b)** **(c)** **(d)**

Figure A.3: Point phantom simulation with compression ratio of 0.9 and standoff pad thickness of 15 mm. (a) Reference simulation. (b) Gran Decoded. (c) Compressed Sensing Decoded. (d) Compressed Sensing Partial Decoded.

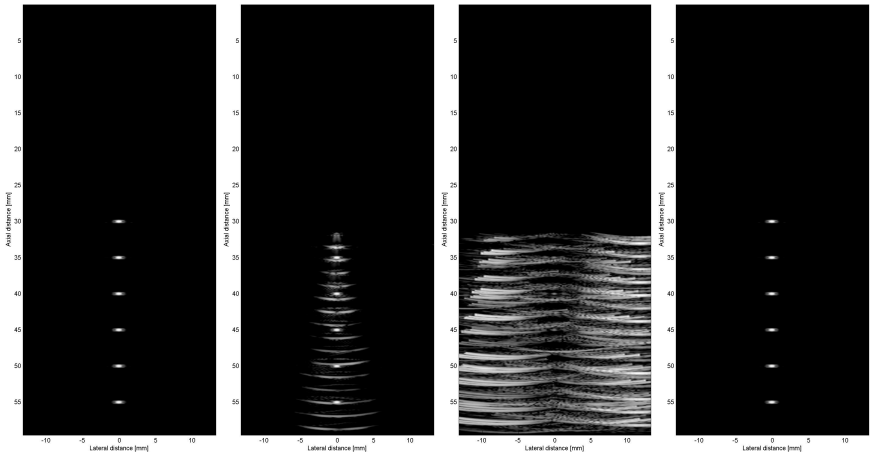

(a) **(b)** **(c)** **(d)**

Figure A.4: Point phantom simulation with compression ratio of 0.9 and standoff pad thickness of 30 mm. (a) Reference simulation. (b) Gran Decoded. (c) Compressed Sensing Decoded. (d) Compressed Sensing Partial Decoded.

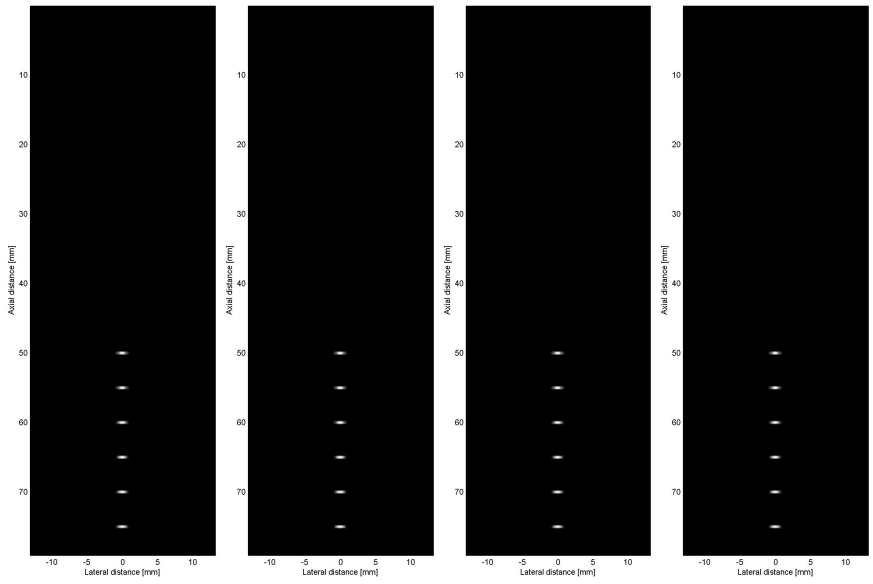

(a) **(b)** **(c)** **(d)**

Figure A.5: Point phantom simulation with compression ratio of 0.9 and standoff pad thickness of 50 mm. (a) Reference simulation. (b) Gran Decoded. (c) Compressed Sensing Decoded. (d) Compressed Sensing Partial Decoded.

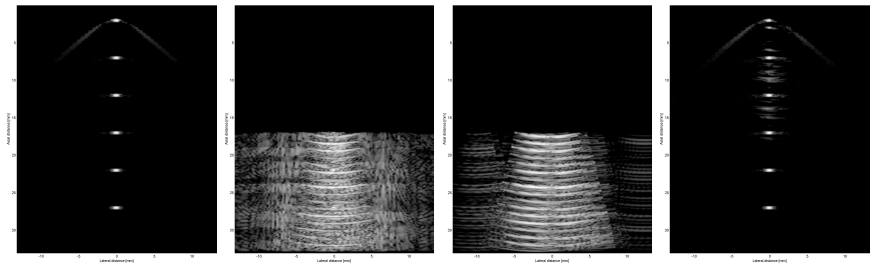

(a) **(b)** **(c)** **(d)**

Figure A.6: Point phantom simulation with compression ratio of 1 and standoff pad thickness of 2 mm. (a) Reference simulation. (b) Gran Decoded. (c) Compressed Sensing Decoded. (d) Compressed Sensing Partial Decoded.

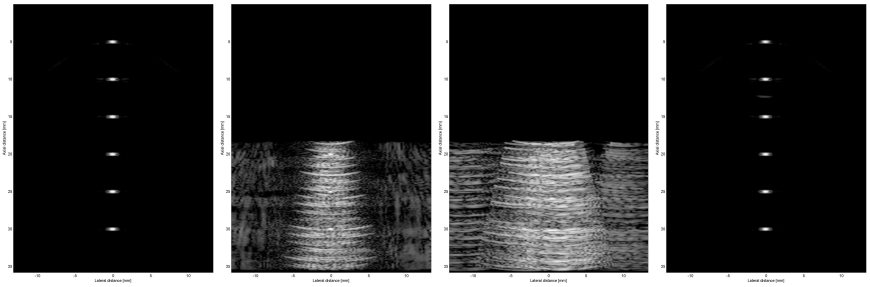

(a) **(b)** **(c)** **(d)**

Figure A.7: Point phantom simulation with compression ratio of 1 and stand-off pad thickness of 5 mm. (a) Reference simulation. (b) Gran Decoded. (c) Compressed Sensing Decoded. (d) Compressed Sensing Partial Decoded.

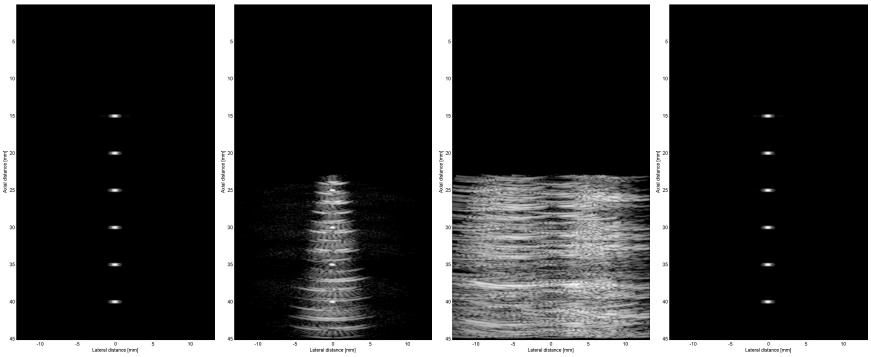

(a) **(b)** **(c)** **(d)**

Figure A.8: Point phantom simulation with compression ratio of 1 and stand-off pad thickness of 15 mm. (a) Reference simulation. (b) Gran Decoded. (c) Compressed Sensing Decoded. (d) Compressed Sensing Partial Decoded.

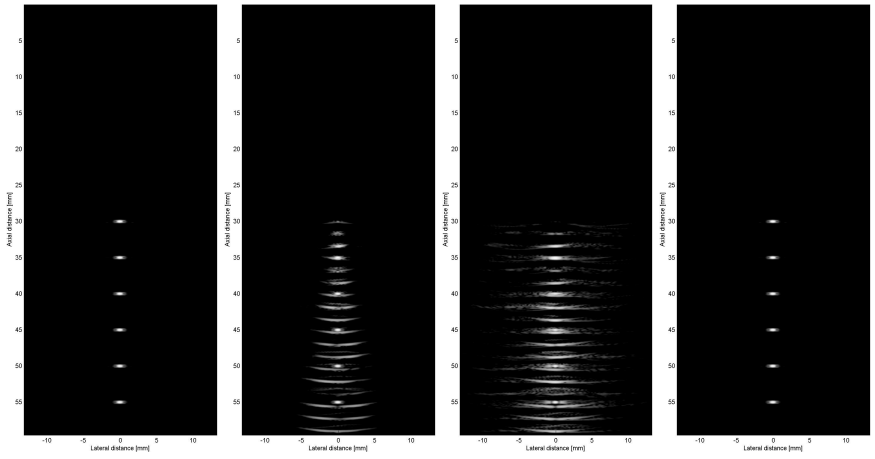

Figure A.9: Point phantom simulation with compression ratio of 1 and stand-off pad thickness of 30 mm. (a) Reference simulation. (b) Gran Decoded. (c) Compressed Sensing Decoded. (d) Compressed Sensing Partial Decoded.

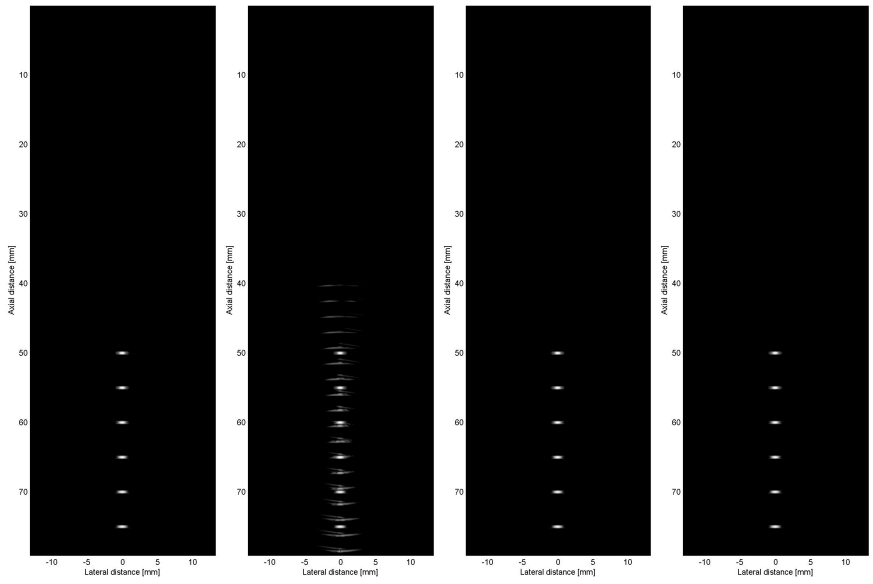

(a) **(b)** **(c)** **(d)**

Figure A.10: Point phantom simulation with compression ratio of 1 and standoff pad thickness of 50 mm. (a) Reference simulation. (b) Gran Decoded. (c) Compressed Sensing Decoded. (d) Compressed Sensing Partial Decoded.

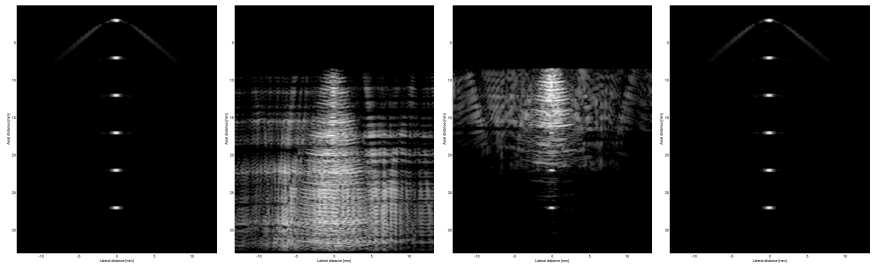

(a) **(b)** **(c)** **(d)**

Figure A.11: Point phantom simulation with compression ratio of 3 and standoff pad thickness of 2 mm. (a) Reference simulation. (b) Gran Decoded. (c) Compressed Sensing Decoded. (d) Compressed Sensing Partial Decoded.

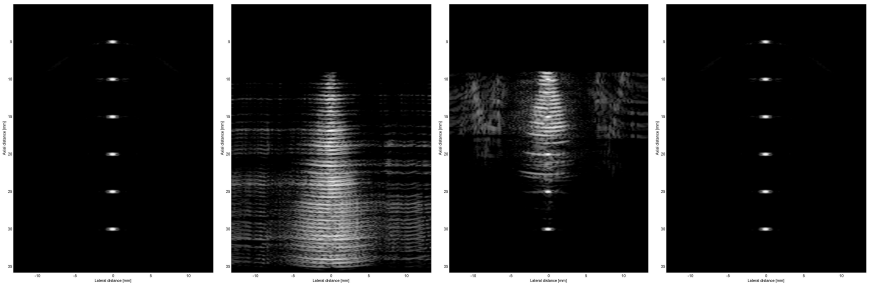

(a) **(b)** **(c)** **(d)**

Figure A.12: Point phantom simulation with compression ratio of 3 and standoff pad thickness of 5 mm. (a) Reference simulation. (b) Gran Decoded. (c) Compressed Sensing Decoded. (d) Compressed Sensing Partial Decoded.

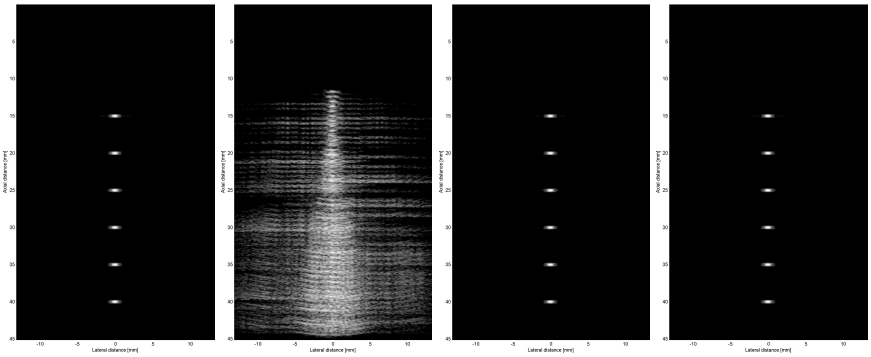

(a) **(b)** **(c)** **(d)**

Figure A.13: Point phantom simulation with compression ratio of 3 and standoff pad thickness of 15 mm. (a) Reference simulation. (b) Gran Decoded. (c) Compressed Sensing Decoded. (d) Compressed Sensing Partial Decoded.

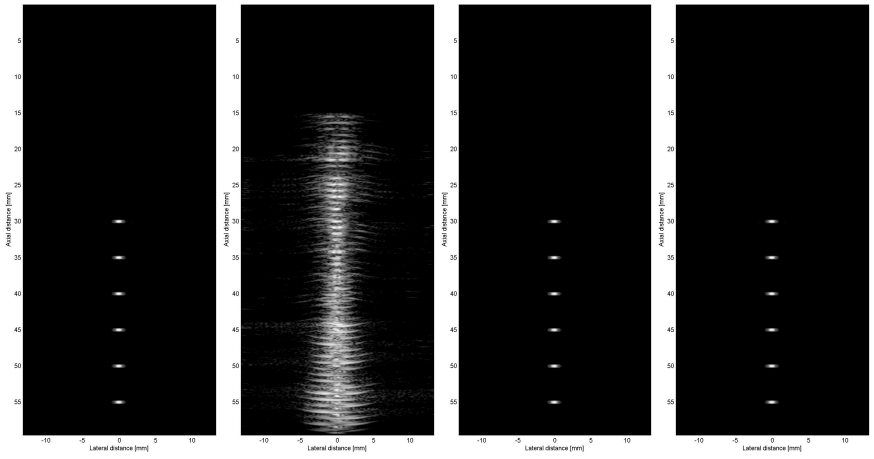

(a) **(b)** **(c)** **(d)**

Figure A.14: Point phantom simulation with compression ratio of 3 and standoff pad thickness of 30 mm. (a) Reference simulation. (b) Gran Decoded. (c) Compressed Sensing Decoded. (d) Compressed Sensing Partial Decoded.

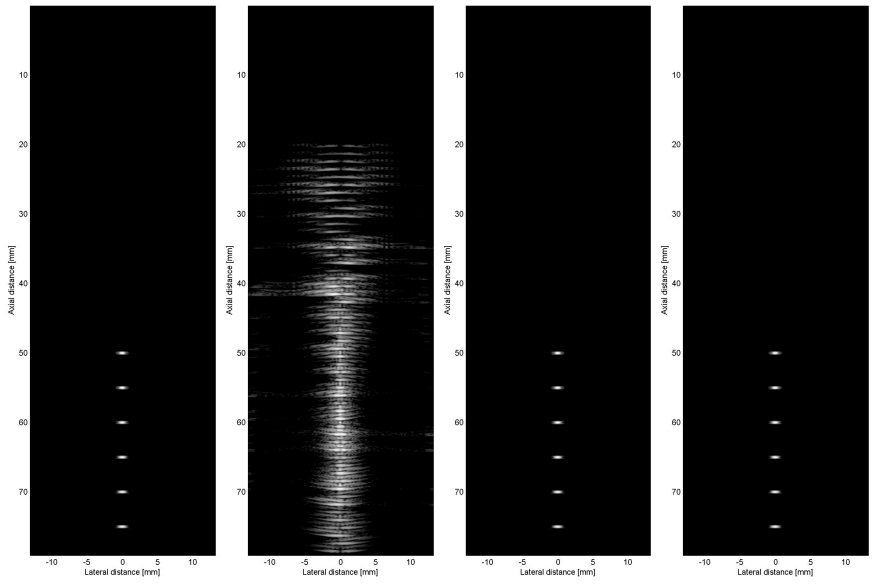

(a) **(b)** **(c)** **(d)**

Figure A.15: Point phantom simulation with compression ratio of 3 and standoff pad thickness of 50 mm. (a) Reference simulation. (b) Gran Decoded. (c) Compressed Sensing Decoded. (d) Compressed Sensing Partial Decoded.

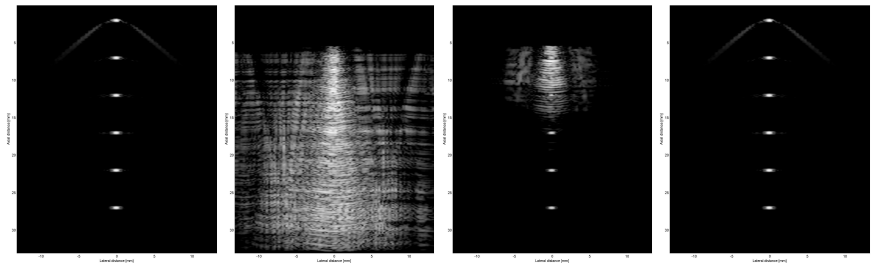

(a) **(b)** **(c)** **(d)**

Figure A.16: Point phantom simulation with compression ratio of 5 and standoff pad thickness of 2 mm. (a) Reference simulation. (b) Gran Decoded. (c) Compressed Sensing Decoded. (d) Compressed Sensing Partial Decoded.

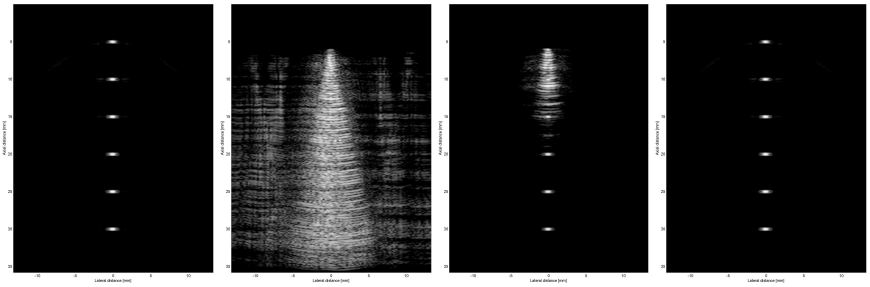

(a) **(b)** **(c)** **(d)**

Figure A.17: Point phantom simulation with compression ratio of 5 and standoff pad thickness of 5 mm. (a) Reference simulation. (b) Gran Decoded. (c) Compressed Sensing Decoded. (d) Compressed Sensing Partial Decoded.

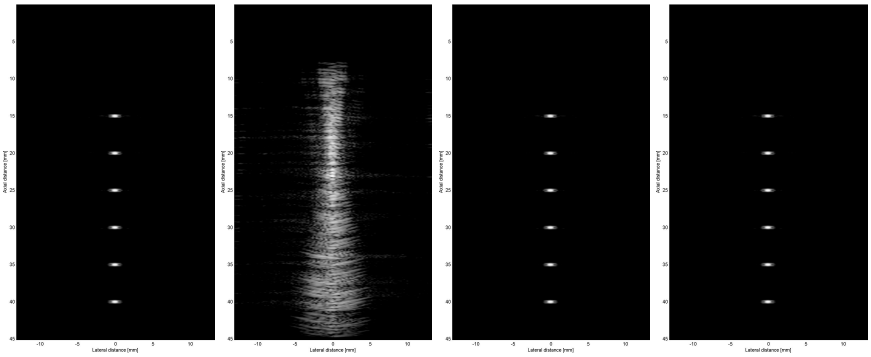

(a) **(b)** **(c)** **(d)**

Figure A.18: Point phantom simulation with compression ratio of 5 and standoff pad thickness of 15 mm. (a) Reference simulation. (b) Gran Decoded. (c) Compressed Sensing Decoded. (d) Compressed Sensing Partial Decoded.

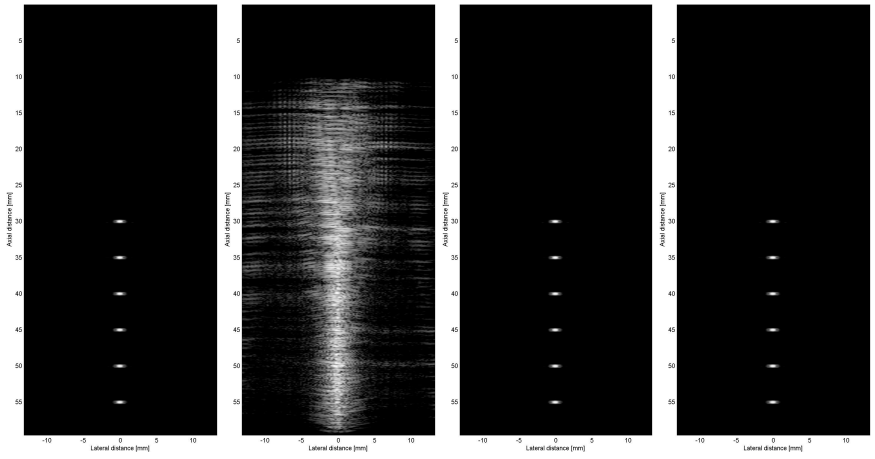

(a) **(b)** **(c)** **(d)**

Figure A.19: Point phantom simulation with compression ratio of 5 and standoff pad thickness of 30 mm. (a) Reference simulation. (b) Gran Decoded. (c) Compressed Sensing Decoded. (d) Compressed Sensing Partial Decoded.

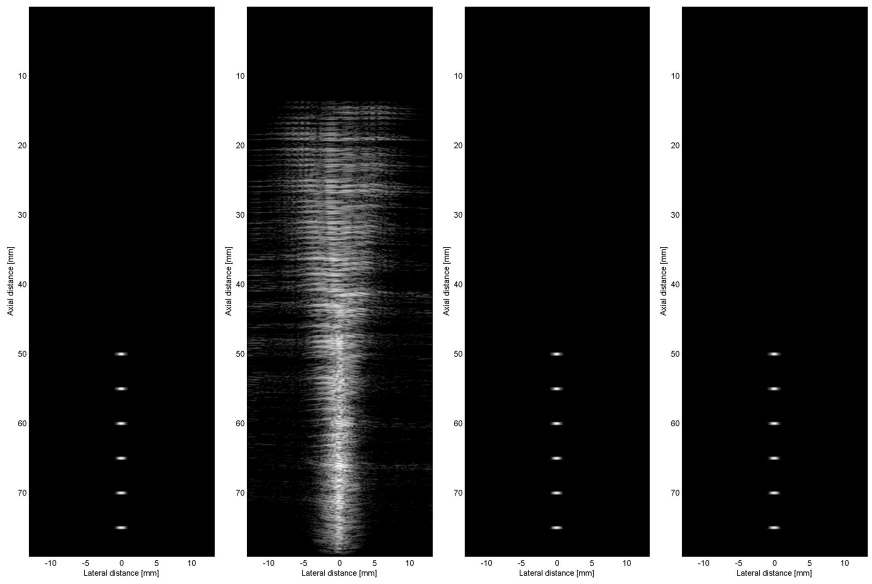

Figure A.20: Point phantom simulation with compression ratio of 5 and standoff pad thickness of 50 mm. (a) Reference simulation. (b) Gran Decoded. (c) Compressed Sensing Decoded. (d) Compressed Sensing Partial Decoded.

Appendix B

Compressed Sensing Tissue Phantom Images

This appendix contains the resulting images from the 20 simulations conducted on the tissue phantom (Section 5.5) for each combination of compression ratios 0.9, 1, 3, 5 and standoff pad thicknesses of 2mm, 5mm, 15mm, 30mm, 50mm.

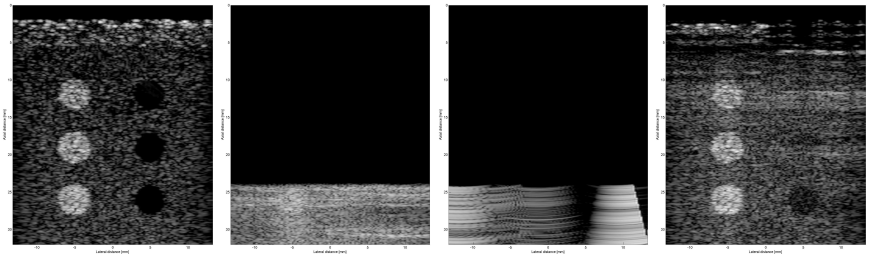

(a) **(b)** **(c)** **(d)**

Figure B.1: Tissue phantom simulation with compression ratio of 0.9 and standoff pad thickness of 2 mm. (a) Reference simulation. (b) Gran Decoded. (c) Compressed Sensing Decoded. (d) Compressed Sensing Partial Decoded.

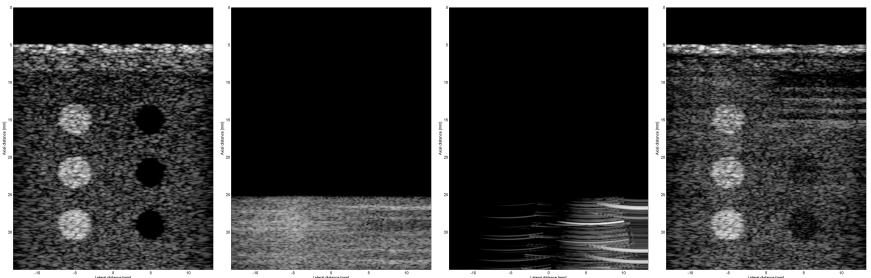

(a) **(b)** **(c)** **(d)**

Figure B.2: Tissue phantom simulation with compression ratio of 0.9 and standoff pad thickness of 5 mm. (a) Reference simulation. (b) Gran Decoded. (c) Compressed Sensing Decoded. (d) Compressed Sensing Partial Decoded.

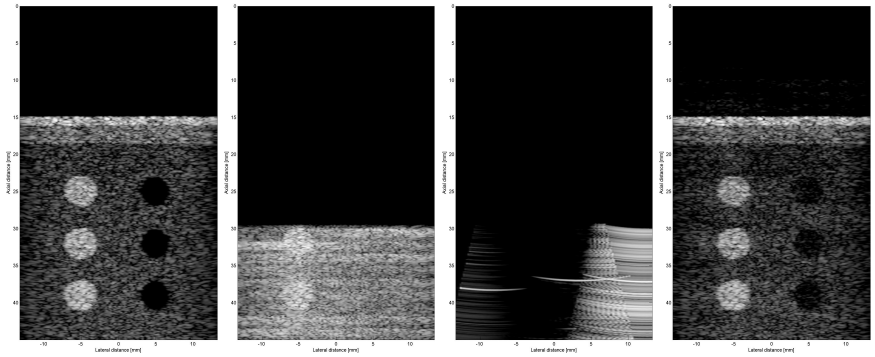

(a) **(b)** **(c)** **(d)**

Figure B.3: Tissue phantom simulation with compression ratio of 0.9 and standoff pad thickness of 15 mm. (a) Reference simulation. (b) Gran Decoded. (c) Compressed Sensing Decoded. (d) Compressed Sensing Partial Decoded.

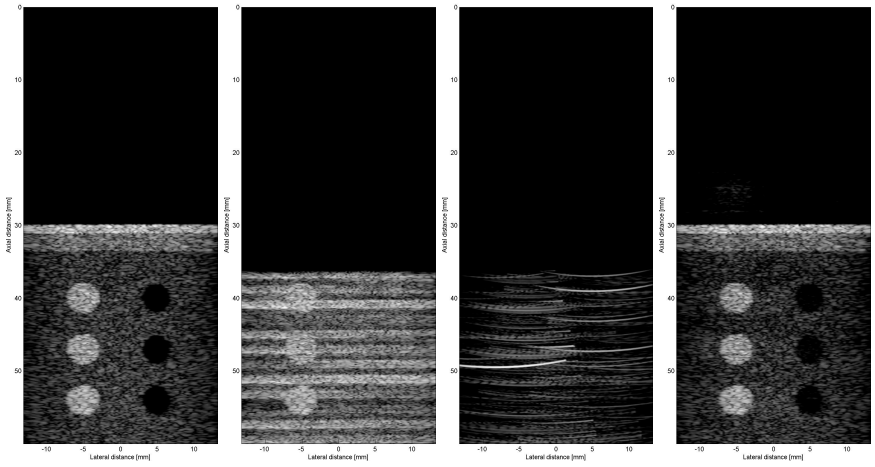

(a) **(b)** **(c)** **(d)**

Figure B.4: Tissue phantom simulation with compression ratio of 0.9 and standoff pad thickness of 30 mm. (a) Reference simulation. (b) Gran Decoded. (c) Compressed Sensing Decoded. (d) Compressed Sensing Partial Decoded.

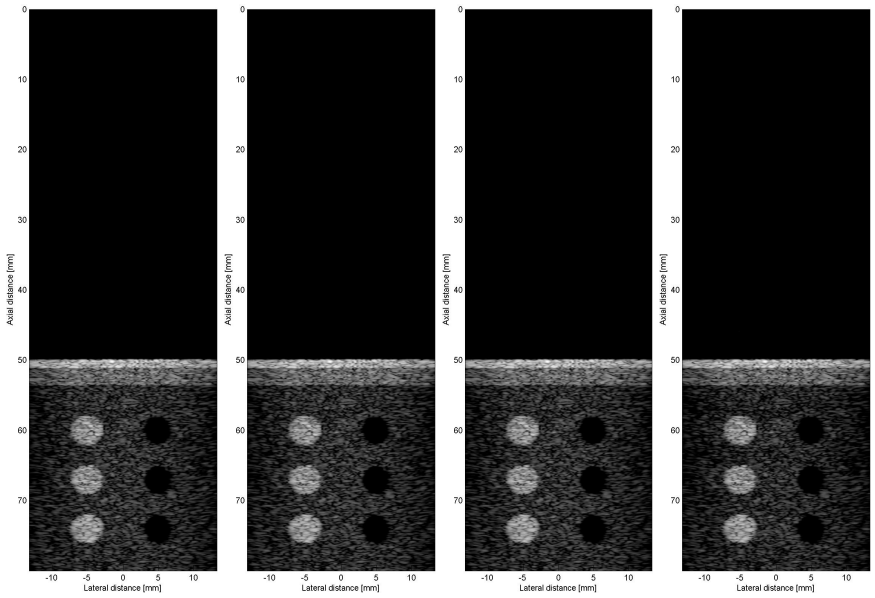

(a) **(b)** **(c)** **(d)**

Figure B.5: Tissue phantom simulation with compression ratio of 0.9 and standoff pad thickness of 50 mm. (a) Reference simulation. (b) Gran Decoded. (c) Compressed Sensing Decoded. (d) Compressed Sensing Partial Decoded.

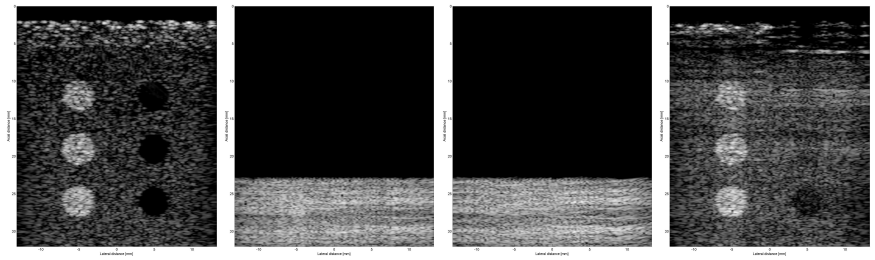

(a) **(b)** **(c)** **(d)**

Figure B.6: Tissue phantom simulation with compression ratio of 1 and standoff pad thickness of 2 mm. (a) Reference simulation. (b) Gran Decoded. (c) Compressed Sensing Decoded. (d) Compressed Sensing Partial Decoded.

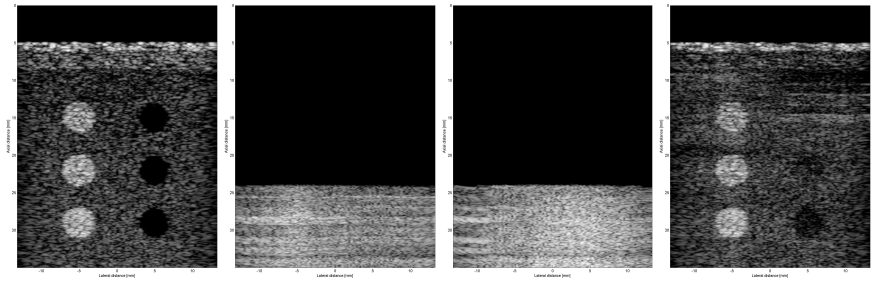

(a) **(b)** **(c)** **(d)**

Figure B.7: Tissue phantom simulation with compression ratio of 1 and standoff pad thickness of 5 mm. (a) Reference simulation. (b) Gran Decoded. (c) Compressed Sensing Decoded. (d) Compressed Sensing Partial Decoded.

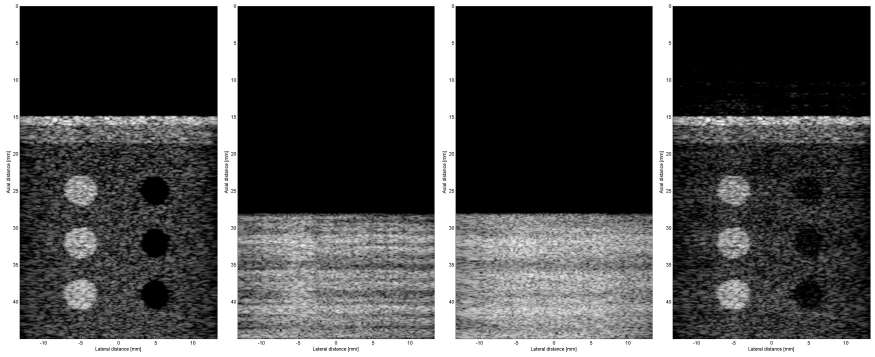

(a) **(b)** **(c)** **(d)**

Figure B.8: Tissue phantom simulation with compression ratio of 1 and standoff pad thickness of 15 mm. (a) Reference simulation. (b) Gran Decoded. (c) Compressed Sensing Decoded. (d) Compressed Sensing Partial Decoded.

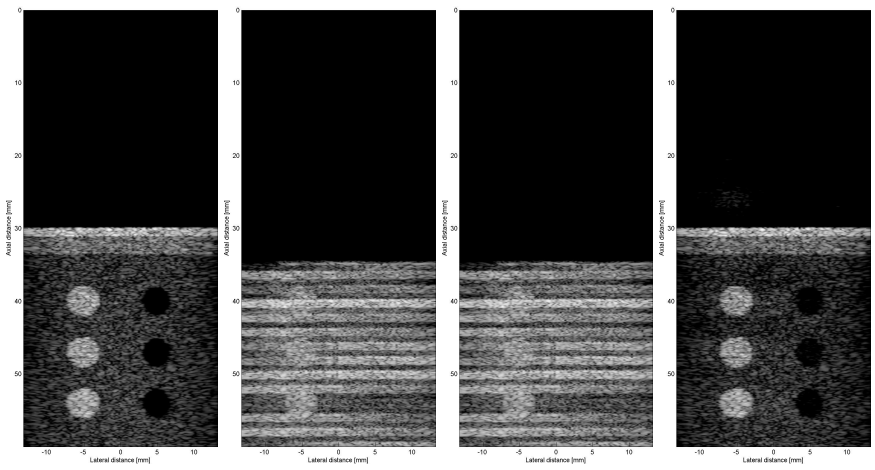

(a) **(b)** **(c)** **(d)**

Figure B.9: Tissue phantom simulation with compression ratio of 1 and standoff pad thickness of 30 mm. (a) Reference simulation. (b) Gran Decoded. (c) Compressed Sensing Decoded. (d) Compressed Sensing Partial Decoded.

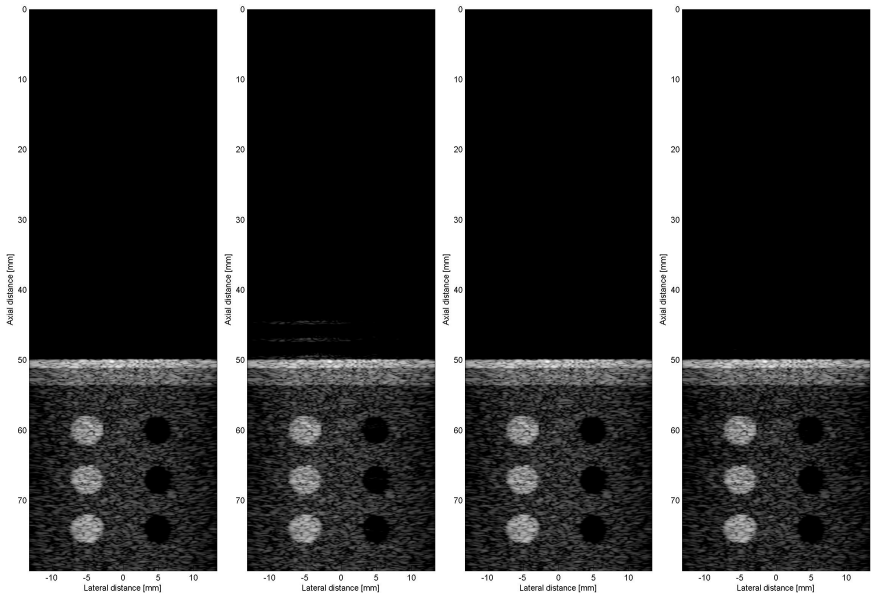

(a) **(b)** **(c)** **(d)**

Figure B.10: Tissue phantom simulation with compression ratio of 1 and standoff pad thickness of 50 mm. (a) Reference simulation. (b) Gran Decoded. (c) Compressed Sensing Decoded. (d) Compressed Sensing Partial Decoded.

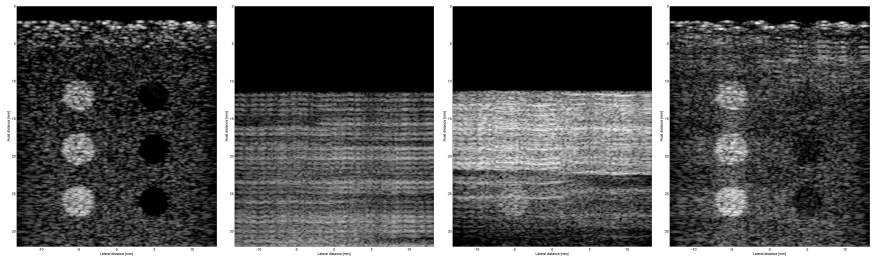

(a) **(b)** **(c)** **(d)**

Figure B.11: Tissue phantom simulation with compression ratio of 3 and standoff pad thickness of 2 mm. (a) Reference simulation. (b) Gran Decoded. (c) Compressed Sensing Decoded. (d) Compressed Sensing Partial Decoded.

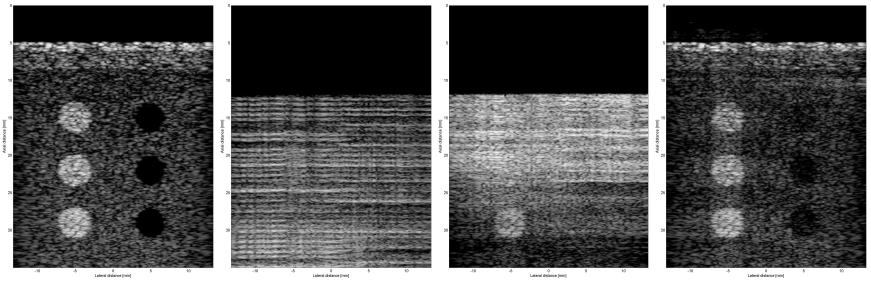

(a) **(b)** **(c)** **(d)**

Figure B.12: Tissue phantom simulation with compression ratio of 3 and standoff pad thickness of 5 mm. (a) Reference simulation. (b) Gran Decoded. (c) Compressed Sensing Decoded. (d) Compressed Sensing Partial Decoded.

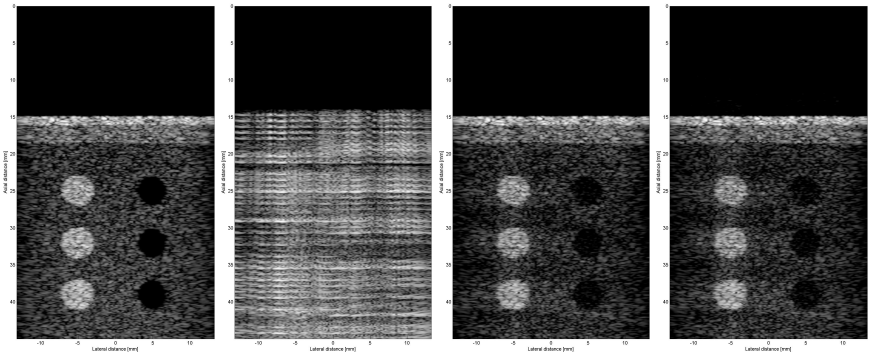

(a) **(b)** **(c)** **(d)**

Figure B.13: Tissue phantom simulation with compression ratio of 3 and standoff pad thickness of 15 mm. (a) Reference simulation. (b) Gran Decoded. (c) Compressed Sensing Decoded. (d) Compressed Sensing Partial Decoded.

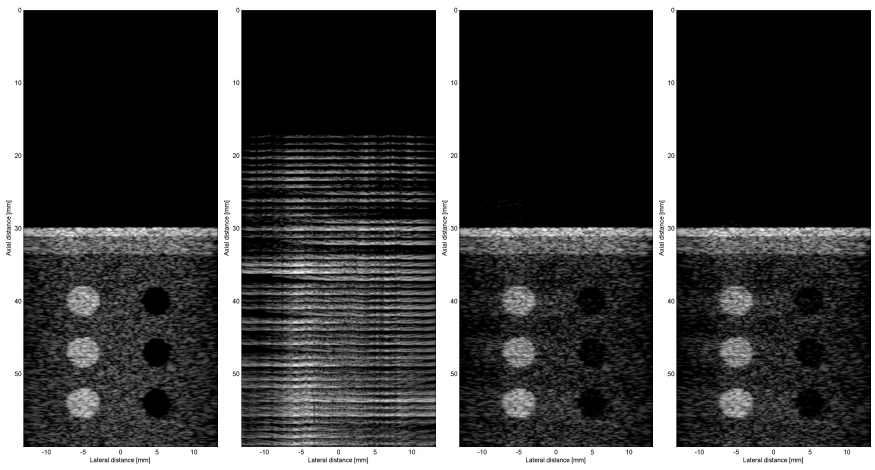

(a) **(b)** **(c)** **(d)**

Figure B.14: Tissue phantom simulation with compression ratio of 3 and standoff pad thickness of 30 mm. (a) Reference simulation. (b) Gran Decoded. (c) Compressed Sensing Decoded. (d) Compressed Sensing Partial Decoded.

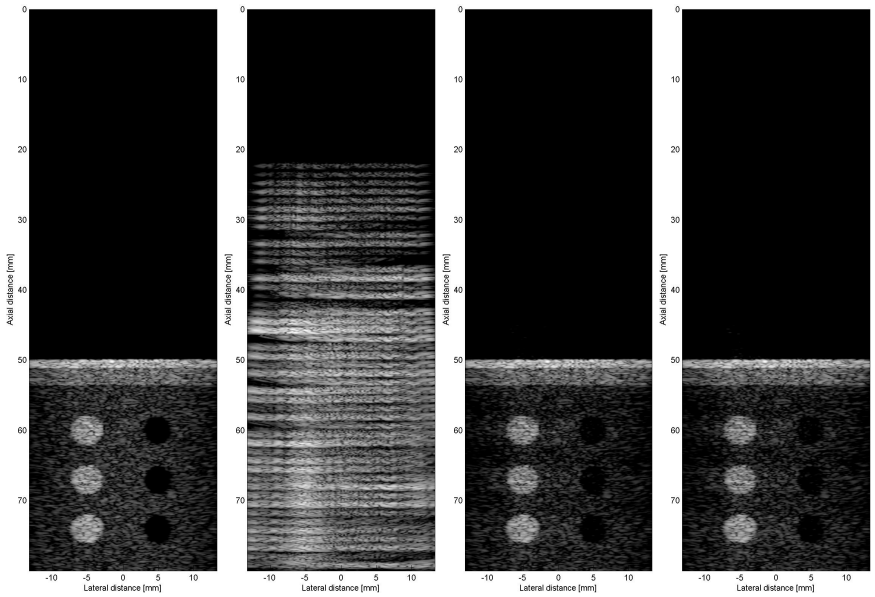

(a) **(b)** **(c)** **(d)**

Figure B.15: Tissue phantom simulation with compression ratio of 3 and standoff pad thickness of 50 mm. (a) Reference simulation. (b) Gran Decoded. (c) Compressed Sensing Decoded. (d) Compressed Sensing Partial Decoded.

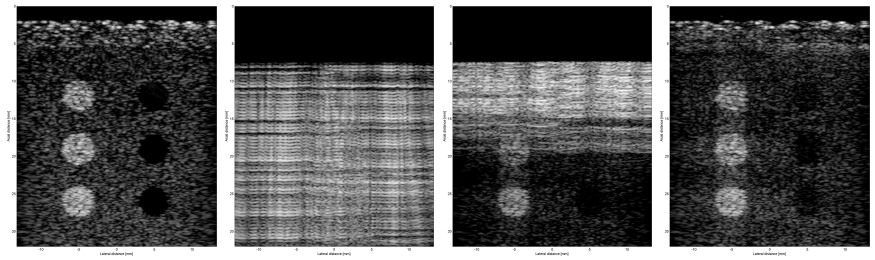

(a) **(b)** **(c)** **(d)**

Figure B.16: Tissue phantom simulation with compression ratio of 5 and standoff pad thickness of 2 mm. (a) Reference simulation. (b) Gran Decoded. (c) Compressed Sensing Decoded. (d) Compressed Sensing Partial Decoded.

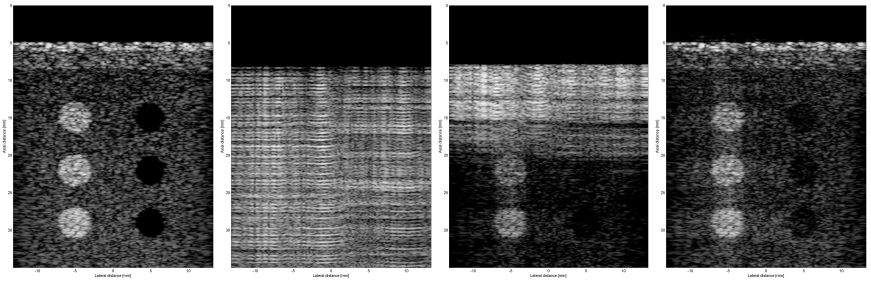

(a) **(b)** **(c)** **(d)**

Figure B.17: Tissue phantom simulation with compression ratio of 5 and standoff pad thickness of 5 mm. (a) Reference simulation. (b) Gran Decoded. (c) Compressed Sensing Decoded. (d) Compressed Sensing Partial Decoded.

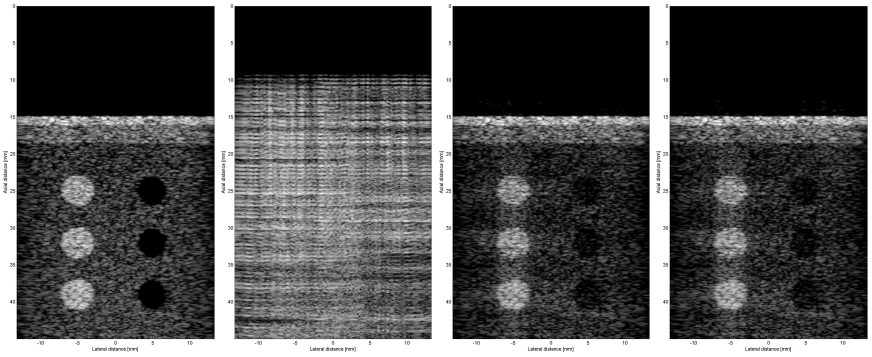

(a) **(b)** **(c)** **(d)**

Figure B.18: Tissue phantom simulation with compression ratio of 5 and standoff pad thickness of 15 mm. (a) Reference simulation. (b) Gran Decoded. (c) Compressed Sensing Decoded. (d) Compressed Sensing Partial Decoded.

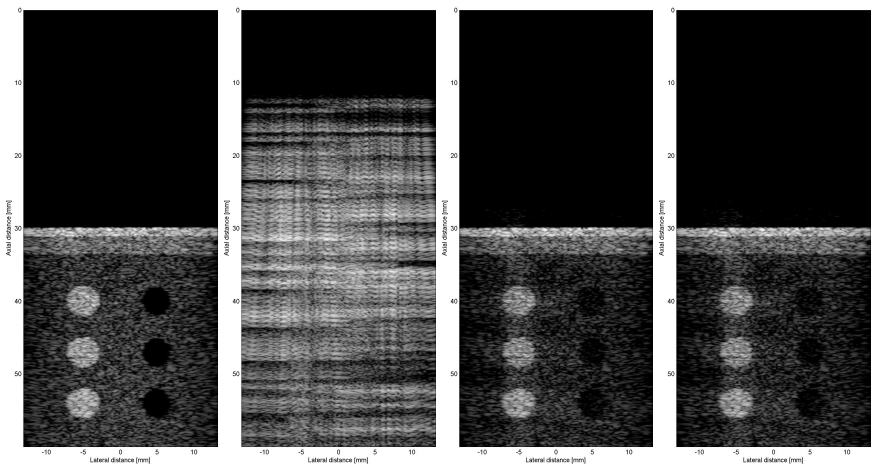

(a) **(b)** **(c)** **(d)**

Figure B.19: Tissue phantom simulation with compression ratio of 5 and standoff pad thickness of 30 mm. (a) Reference simulation. (b) Gran Decoded. (c) Compressed Sensing Decoded. (d) Compressed Sensing Partial Decoded.

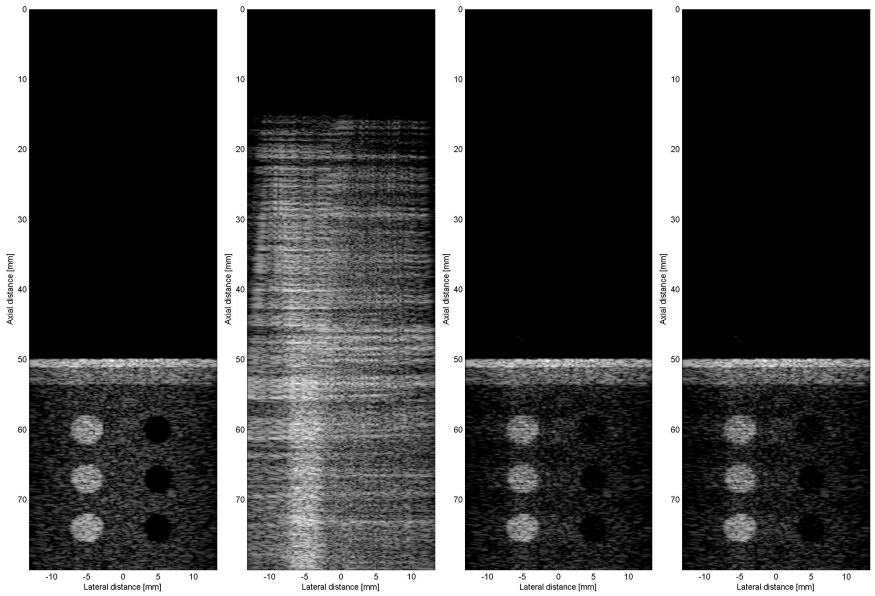

Figure B.20: Tissue phantom simulation with compression ratio of 5 and standoff pad thickness of 50 mm. (a) Reference simulation. (b) Gran Decoded. (c) Compressed Sensing Decoded. (d) Compressed Sensing Partial Decoded.